Homoclinic tangles-classification and applications

1994 Nonlinearity 7 441

(http://iopscience.iop.org/0951-7715/7/2/008)

Nonlinearity 7 (1994) 441–473. Printed in the UK

Homoclinic tangles—classification and applications

Vered Rom-Kedar†

The Department of Applied Mathematics and Computer Science, The Weizmann Institute of Science, PO Box 26, Rehovot 76100, Israel

Received 27 November 1992, in final form 11 October 1993
Recommended by I Stewart

Abstract. Here we develop the Topological Approximation Method (TAM) which gives a new description of the mixing and transport processes in chaotic two-dimensional time-periodic Hamiltonian flows. It is based upon the structure of the homoclinic tangle, and supplies a detailed solution to a transport problem for this class of systems, the characteristics of which are typical to chaotic, yet not ergodic dynamical systems. These characteristics suggest some new criteria for quantifying transport and mixing—hence chaos—in such systems. The results depend on several parameters, which are found by perturbation analysis in the near integrable case, and numerically otherwise. The strength of the method is demonstrated on a simple model. We construct a bifurcation diagram describing the changes in the homoclinic tangle as the physical parameters are varied. From this diagram we find special regions in the parameter space in which we approximate the escape rates from the vicinity of the homoclinic tangle, finding non-trivial self-similar solutions as the forcing magnitude tends to zero. We compare the theoretical predictions with brute force calculations of the escape rates, and obtain satisfactory agreement.

AMS classification scheme numbers: 58F14, 58F13, 58F30, 70K05, 70K50

1. Introduction

Until recently, it has been fashionable to numerically find that the model in question is chaotic, at best prove it, and skip to the next model. However, by now it is well known that most flows in nature are chaotic, thereby nullifying the above exercise. Instead, developing tools to quantify the behaviour of ensembles of solutions to chaotic flows is on the agenda. For example, two significant properties that all chaotic flows present are enhanced transport and exponential stretching of material lines. Beyond their theoretical value as quantifiers of chaos, both properties are important in applications [1–6]: studying the spread of pollution due to simple time-dependent velocity fields, and studying chemical reaction rate between two fluids in motion must be preceded by an analysis of the transport rates and the interface growth rate, respectively.

The underlying structure which determines the transport properties of the considered mappings‡ is the homoclinic tangle (see figure 2 below). It is created by the intersections of stable and unstable manifolds of the mappings' hyperbolic fixed points. Since both manifolds are invariant, once they intersect at a point, they must intersect at all its forward and backward iterates. As line elements are also stretched in the vicinity of the hyperbolic

† Part of this research was conducted while the author was a member of the Computational and Applied Mathematics Program, The Department of Mathematics, The University of Chicago.

‡ The mapping may be the Poincaré map of a time-periodic flow constructed by sampling the flows solutions at constant intervals of times, corresponding to the periodicity of the vector field.

point, the consequence of an intersection of the manifolds is the homoclinic tangle. Using the Smale–Birkhoff homoclinic theorem, the existence of a homoclinic tangle has been extensively used for proving that a given flow is chaotic. However, the chaos occurs on a measure zero set, which is unobservable. Analysing the transport corresponds to analysing the dynamics of the complement set to this chaotic invariant set.

The methods we use here are reminiscent of methods used in studies of scattering [7, 8]. In these one usually constructs symbolic dynamics which is in one to one correspondence with the trajectories of a hyperbolic invariant set. The hyperbolic structure of the invariant set enables one to predict the asymptotic behaviour of the system. However, the situation is more complicated when the system is mixed, containing both hyperbolic and elliptic structures. Traditionally, people have attacked the mixed problem using the 'effective diffusion' concept. Diffusion and transport were used almost as synonyms, and the criterion for a successful transport model was its capability to predict the diffusion coefficient in the system. In the last decade, it has been realized that transport (conveying 'particles' from one region to another) may be governed by non-diffusive processes for which the diffusion coefficient is ill-defined [9–12]. The first non-diffusive model for transport in chaotic systems was introduced a decade ago by MacKay *et al* [10]. Their general ideas were used in numerous subsequent works on the subject (see the review by Meiss [13]) and inspired the finding of important scaling properties of partial barriers to the flow [10, 14]. However, several key assumptions (such as 'loss of memory' in subregions of the flow) are, in our view, inconsistent with the structure of chaotic flows [15, 16].

Here we develop an alternative non-diffusive nonlocal transport model: the TAM (Topological Approximation Method) supplies a new transport mechanism for two-dimensional area-preserving chaotic maps. The transport model depends on several parameters which are determined by the geometry of the homoclinic tangle. These are the Transport Order Parameters (TOP) of the map or flow [17]. We develop an analytical method to estimate the TOP for a class of near integrable Hamiltonian systems. Otherwise, these parameters may be found numerically. The critical assumption of the TAM is the simplicity of the topological structure of the manifolds, based upon simple templates or the 'Birkhoff signature' of the tangle [18, 19]. As a by-product, the TAM supplies a lower bound on the stretching of material lines (mixing). Judd [20] noted that their asymptotic behaviour gives a lower bound on the topological entropy, and developed independently similar ideas for estimating the topological entropy and the Hausdorf dimension of the unstable manifold of dissipative homoclinic tangles.

Another tradition in the dynamical system community, which we do not follow, is to characterize solely the asymptotic behaviour of solutions. First, in many applications *finite* time results are significant [21]. Second, in many chaotic dynamical systems the transient behaviour is long, hence theoretical characterization of the transience is as important as a characterization of the asymptotic behaviour. Third, in some cases the asymptotic behaviour depends sensitively on the ensemble one takes and on the time interval one considers, hence it is not well defined. The TAM predicts both finite and infinite time behaviour. We believe its main contribution is in the finite time results, which lead to new characterizations of the transient behaviour, and may be rigorously justified.

The TAM may be applied to two-dimensional area-preserving maps (possibly a Poincaré map of a flow) satisfying the following three assumptions:

(1A) The map possesses a hyperbolic fixed point p.

(1B) The stable (respectively unstable) manifold of p has one branch which intersects the unstable (respectively stable) manifold transversely†.

(1C) The map is an *open map*: the other branch of the stable (respectively unstable) manifold of p extends to infinity, possessing no homoclinic orbits.

For simplicity of notation we assume in (1A)–(1C) that the tangle is homoclinic (associated with the intersection of the stable and unstable manifolds of a *single* hyperbolic fixed point p). However, the results can be easily extended to the heteroclinic case. The most significant assumption we make on the flow is (1C)—that of open flow. It implies that there is only one tangle of the stable and unstable manifolds, and hence there is no mechanism for re-entrainment. There are several reasons for considering these flows. Physically, they come up in applications, e.g. pollution problems in the context of fluid mechanics and ionization problems in the context of chemical reactions. Mathematically these systems are interesting since they are inherently transient (their asymptotic behaviour is quite boring), hence the concepts of finite time estimates must be developed. These concepts may subsequently be used to characterize the transient behaviour of closed chaotic systems. Finally, these flows are simpler to investigate theoretically and numerically, hence they serve as good building blocks and as test problems for advanced methods. Indeed, the TAM has been recently generalized to closed flows as well [17], so classical examples like the forced Duffing equation and the forced pendulum may be similarly analysed.

This paper is organized as follows: in section 2 we present our model and verify that it satisfies the open flow assumption and the assumptions required for applying the perturbation analysis. In section 3 we introduce the notation for classifying the homoclinic tangles and define the quantities we estimate in this paper. We end this section with a definition of some of the geometrical parameters of the homoclinic tangle. In section 4 we compute the whisker map for our model and use it to estimate the geometrical parameters which were defined in section 3. The results are summarized in a bifurcation diagram, which describes the dependence of the geometrical parameters on (ϵ, ω). In section 5, we summarize some of the methods developed by Rom-Kedar [22] for estimating the development of tangles in specific regions of the parameter space. Then, we use this construction to estimate the exponential growth rate of line elements for our example and find the beginning of a Devil's Staircase for the topological entropy. In section 6, we estimate the escape rates for these tangles using the whisker map and the TAM, examine their behaviour in the limit of small ϵ, and end this section with a comparison to brute force computation. Section 7 contains a summary and a discussion of the results. In appendix A, which summarizes a joint work with Dana Hobson, we present a numerical bifurcation diagram and a description of the numerical method we use to find it. In appendix B we include some details of a calculation of the geometrical parameters. In appendix C we derive the approximate action formulae and estimate the initial escape rates.

2. A particle in a cubic potential

To demonstrate our theory, we study the phase space flow of a particle in a forced cubic potential, with the Hamiltonian:

$$H_\epsilon(x, y, t) = \tfrac{1}{2}y^2 + (\tfrac{1}{2}x^2 - \tfrac{1}{3}x^3 - \tfrac{1}{6})(1 + \varepsilon\cos(\omega t)) \tag{2.1}$$

where ϵ and ω are the two non-dimensional parameters, measuring, respectively, the strength and frequency of the forcing. This problem has direct applications in mechanics and

† The orbits along which the stable and unstable manifolds intersect are called homoclinic orbits.

chemistry and may also be considered the normal form of a more complicated Hamiltonian system. We verify that for $\varepsilon \neq 0$, the Hamiltonian (2.1) gives rise to a system which satisfies assumptions (1A)–(1C). The Hamiltonian (2.1) induces the flow:

$$\begin{aligned}\frac{\mathrm{d}x}{\mathrm{d}t} &= y \\ \frac{\mathrm{d}y}{\mathrm{d}t} &= x(x-1)(1+\varepsilon\cos(\omega t)).\end{aligned} \tag{2.2}$$

For all ε, the points $(0,0)$ and $(1,0)$ are fixed points of (2.2). When $\varepsilon = 0$, the fixed point $(1,0)$ is hyperbolic, hence for sufficiently small ϵ $(1,0)$ remains hyperbolic and assumption (1A) is satisfied. For the unperturbed system, assumption (1C) holds, and one can prove that for sufficiently small ϵ the perturbed system must satisfy (1C) as well. Finally, for $\epsilon = 0$, the parts of the stable and unstable manifolds which do not extend to infinity coincide. To prove that (1B) holds for $\epsilon \neq 0$, we calculate the Melnikov function and verify that it has simple zeros [23, 24]. Solving (2.2) for the unperturbed homoclinic orbit, we compute the Melnikov function $M(t_0)$:

$$M(t_0) = \int_{-\infty}^{\infty} y\ (-x+x^2)\cos(\omega(t+t_0))\Big|_{\text{homoclinic orbit}} \mathrm{d}t = C(\omega)\sin(\omega t_0) \tag{2.3}$$

where

$$C(\omega) = \tfrac{3}{5}\pi\omega^2(1-\omega^4)\,\mathrm{cosech}(\pi\omega). \tag{2.4}$$

The function $C(\omega)$ is plotted in figure 1. Notice that $C(\omega) = 0$ when $\omega = 1$ and when $\omega \to 0, \infty$. Therefore, the analysis in this paper applies to small ϵ values and all finite values of ω, excluding neighbourhoods of 0 and 1. We discuss the possible behaviour near these special values of ω in the conclusion section.

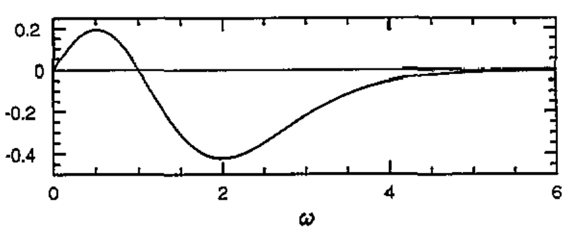

Figure 1. The maximal magnitude of the Melnikov function.

$P(H_0)$, the period of the unperturbed periodic orbits which are foliated in the homoclinic loop is given by:

$$P(H_0) = \sqrt{6}\int_c^b \frac{\mathrm{d}q}{\sqrt{(q-1)^2(q+\frac{1}{2})+3H_0}} \approx \ln\left(\frac{72}{-H_0}\right)(1+O(\sqrt{|H_0|})). \tag{2.5}$$

It follows from (2.2) that for the unperturbed problem H_0 vanishes on the homoclinic orbit, hence near the separatrix, $|H_0| \ll 1$.

It follows from the above calculations that $H_\epsilon(x, y, t)$ is analytic in ϵ near $\epsilon = 0$ and periodic in t, that $H_0(x, y)$ is independent of t, that $H_\epsilon(x, y, t)$ is quadratic in (x, y) near the hyperbolic periodic orbit $(1, 0)$ (in particular $H_\epsilon(1, 0, t) = 0$), that the unperturbed structure satisfies the assumptions required for the Melnikov technique to apply (there exists a homoclinic loop, foliated by periodic orbits), that the Melnikov function has simple zeros and no plateaux, and finally that $P'(h) = \frac{1}{h}(1 + o(h))$ for small h. These are the required conditions for applying the perturbation analysis [25].

3. The geometrical properties of the homoclinic tangle

To study (2.2), we introduce a Poincaré cross section in time and define the Poincaré map, F, as the return map to this cross section. In the following analysis let ϵ be sufficiently small, such that the perturbation analysis applies. Then, F has a hyperbolic fixed point at $p = (1, 0)$ and its stable and unstable manifolds persist. Moreover, since the Melnikov function has two simple zeros every period of the perturbation (equation (2.3)), the Poincaré map F has exactly two *primary intersection points (PIP)* denoted by q_0 and p_0 in figure 2. The segments of the stable and unstable manifolds connecting the fixed point to p_0 define a region, S. We study transport and mixing of an initial uniform distribution in S. The segments of the stable and unstable manifolds connecting p_i† and q_i (resp. q_i and p_{i+1}) bound the regions D_i (resp. E_i) which are called 'lobes'. Their dynamics determines the transport through S. The growth rate of the lengths of their boundaries, $L(E_i)$, $L(D_i)$ with i, gives a lower bound to the elongation rates in the flow.

In figure 2 we draw the homoclinic tangle on the Poincaré section with zero phase, for $\omega > 1$. The form of (2.2) implies that at this cross section the stable manifold is identical to the unstable manifolds reflected about the x-axis. Hence p_0 is located on the x-axis (and indeed $M(0) = 0$). Since $M'(0) < 0$ for $\omega > 1$, the orientation of the manifolds at p_0 is as depicted‡. During our analysis, we will remark on the implications of this model's symmetries on the TAM results.

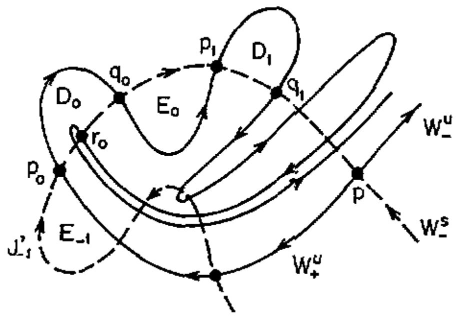

Figure 2. The homoclinic tangle, q_i and p_i are pip orbits. r_i is not.

† $p_i = F^i p_0$.

‡ When $\omega < 1$ this Poincaré map is symmetric about q_0, and the same orientation appears if one considers the Poincaré section for $\omega > 1$ at $t = \pi/\omega$. We note that in practice these values of ω give rise to very large lobes [26], hence we expect that the perturbative tools which we use will not work well in this regime. For simplicity of presentation, we will limit our discussions to the case $\omega > 1$, and quote our *formal* results for $\omega < 1$.

3.1. Transport and mixing characteristics

We define the following characteristics for transport and mixing through the region S:

1. The phase space area originating in S which escapes at the nth iteration:

$$c_n = \mu(F^{n-1}(S) \cap S) - \mu(F^n(S) \cap S)$$

where $\mu(A)$ denotes the area of the set A.

2. The phase space area originating in S which stays in S after the nth iteration:

$$R_n = \mu(F^n(S) \cap S).$$

3. The length of the boundary of $F^n(S)$, $L(F^n(S))$.

The above quantities are independent, up to a shift in n, of the definition of the 'origin' of the orbit p_i (hence S) and of the particular Poincaré section one chooses. When possible, choosing a cross section with symmetries, as in figure 2, is both elegant and computationally efficient. Note that $L(F^n(S))$ is determined by the length of the lobe boundaries $L(E_i)$ and $L(D_i)$. Similarly, in Rom-Kedar *et al* [6] we showed that c_n and R_n can be expressed in terms of the escape rates, e_n, defined by

$$e_n = \mu(E_n \cap D_0).$$

In fact, it is easy to show that for open flows

$$c_n = \mu(D_0) - \sum_{j=1}^{n-1} e_j \qquad R_n = \mu(S) - \sum_{j=1}^{n} c_j. \tag{3.1}$$

The above results are exact and enable a major reduction in computational efforts surrounding the transport rates†. Here we find the mechanisms which govern the behaviour of the e_n's and the $L(E_n)$'s and present an analytical method for estimating them. From the above quantities, we may attempt to extract asymptotic information, for example:

1. The area of the invariant set in S, R_∞.

2. The asymptotic behaviour of c_n for large n; in particular, it is of interest [10, 27] to find whether c_n decays exponentially, as a power law, or in a more complicated fashion in n.

3. The topological entropy, which may be estimated by the asymptotic exponential growth rate of $L(E_n)$,

$$\lambda = \lim_{n\to\infty} \frac{1}{n} \ln L(E_n).$$

† The equivalent formulae for two-dimensional maps which are neither open nor area-preserving have been developed as well.

3.2. Geometrical parameters, tangles and trellises

The topological and metric properties of the flow depend sensitively on the way the homoclinic tangle develops. In general, given the structure of $L(D_0) \cap L(E_j)$, $j = 1, \ldots, n$, one can calculate the *minimal* number of homoclinic points in $L(D_0) \cap L(E_{n+1})$ and their ordering along the stable and unstable manifolds [28]. However, $L(D_0) \cap L(E_{n+1})$ may intersect in other points, which we call spontaneous intersection points [22]. One can imagine that there exist some parameter values for which the arcs do not develop any spontaneous intersection points for all $j > n$. For these parameter values we have some hope of estimating the topological and metric properties accurately, using information regarding the initial development of the manifolds. Then, we would argue that near these parameter values our estimates are still reasonable. This is the basic idea of the TAM. To support these claims, we consider three families of tangles which are determined by geometrical specification for the structure of $L(D_0) \cap L(E_j)$, $j = 1, \ldots, n$, for some finite integer n, and the rule that there are no spontaneous homoclinic points for $j > n$. To specify their structure we first define the *structure indices* ℓ, m, k as follows:

- The structure index ℓ is given by the minimal value of j for which $E_j \cap D_0 \neq \emptyset$.
- The structure index m (respectively k) is given by the minimal value of j for which the intersection of the tip of E_ℓ (respectively $D_{-\ell}$), emanating from $L(D_0)$ (respectively $L(E_0)$), with D_{-j} (respectively E_j) is non-empty.

A tangle belonging to the first family of tangles, the type-ℓ trellises [28], has a structure index ℓ, its critical intersection set, $L(D_0) \cap L(E_\ell)$, contains exactly two homoclinic points (see figure 2), and for $j > \ell$, $L(D_0) \cap L(E_j)$ is determined by the rule that no spontaneous intersection points are allowed. A tangle belonging to the second family of initial configurations, called type-$(\ell, m, k, 0)$ trellises [22], has structure indices ℓ, m, k†, its critical intersection set $L(D_0) \cap L(E_\ell)$ contains exactly four homoclinic points, and the critical intersection sets of the tips contain exactly two intersection points each (see figure 3). If the map is symmetric, as in the figure, then, necessarily, $m = k$. As $m, k \to \infty$ the type-$(\ell, m, k, 0)$ trellises approach the type-ℓ trellis 'from above', namely the tip size decreases as m, k are increased. This feature allows us to examine how the topological and metric properties change as the parameters of the problem vary, suggesting that the topological and metric quantifiers asymptote monotonically their limiting values as one approaches the region of the type-ℓ trellises. Hence our claim, that the estimates should hold in a region of non-vanishing area in parameter space, has some theoretical support. The third family of trellises, of type-$(\ell - 1, s, u, -1)$, may be defined similarly, and approaches the type-$(\ell - 1)$ trellis 'from below': the arc $L(E_{\ell-1})$ grows, intersecting the arcs $L(D_{-s})$, until finally, as $s \to \infty$ it touches the arc $L(D_0)$ and the index ℓ decreases to $\ell - 1$‡. The last of the '0' labelled trellises, the type-$(\ell, \ell - 1, \ell - 1, 0)$ trellis, is identified with the first of the '-1' labelled trellises, the type-$(\ell - 1, \ell - 1, \ell - 1, -1)$ trellis.

We approximate the properties of tangles which have the same structure indices and the same number of homoclinic points in the critical intersection sets by the 'minimal' tangles, the type-ℓ trellises or the type-$(\ell, m, k, 0)$ trellises. In the next section we use the whisker map to find the regions in parameter space in which the tangles satisfy these conditions.

† The last index '0' is a label, indicating which of the three-indices-families of trellises we consider.

‡ The trellis which appears to be most persistent in the Hénon map [29], is a type-$(1, 3, 3, -1)$ trellis.

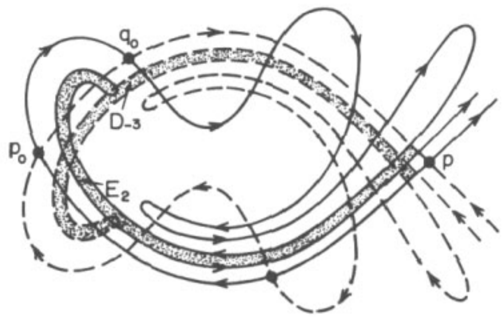

Figure 3. A type-$(\ell, m, k, 0)$ trellis. $\ell = 2$, $m = k = 3$.

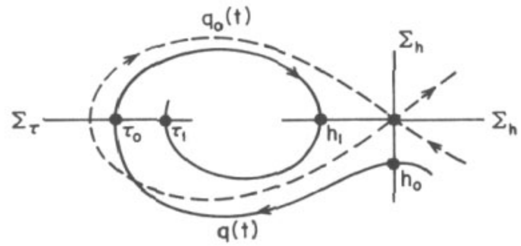

Figure 4. The geometry of the separatrix map. – – –, unperturbed separatrices; ——, an orbit.

4. Calculating the structure indices

In this section we define and compute the whisker map (WM) for (2.2). Then we use it to construct a bifurcation diagram describing the dependence of the structure indices on ϵ and ω.

Define the separatrix map, W, as the return map of the energy and time variables (h_n, τ_n) to the cross sections Σ_h and Σ_τ, respectively (see figure 4):

$$\begin{aligned} &W : (h_n, \tau_n) \to (h_{n+1}, \tau_{n+1}) \\ &q(\tau_n) \in \Sigma_\tau \\ &h_n = H_\epsilon(q(t^*), t^*) \qquad q(t^*) \in \Sigma_h \qquad \tau_n < t^* < \tau_{n+1} \end{aligned} \tag{4.1}$$

where $q(t)$ is a solution to (2.2). In the neighbourhood of the separatrix ($h \ll 1$) the cross sections Σ_h and Σ_τ are transverse to the unperturbed trajectories. Therefore, for sufficiently small ϵ, the separatrix map is well defined there. The WM is defined to be the leading order approximation in ϵ and h to the separatrix map [22], and can be written as [30, 31]:

$$\begin{aligned} h_{n+1} &= h_n + \epsilon M(\tau_n) = h_n + \epsilon C(\omega)\sin(\omega\tau_n) \\ \tau_{n+1} &= \tau_n + P(h_{n+1}) \end{aligned} \tag{4.2}$$

where $C(\omega)$ is defined by (2.4) and $P(h)$ by (2.5). Plugging the approximate expression (2.5) in (4.2) gives rise to the approximate whisker map (AWM) which we have used previously [32]. While the AWM enables one to derive analytical expressions for most of the quantities in question, it introduces a dominant error of order $\sqrt{\epsilon}\ln(\epsilon)$, which limits the applicability of the analysis to much smaller values of ϵ.

Following Escande [3], we argue that for sufficiently small ϵ the sign of h_i determines whether a particle is trapped or not at the ith crossing of Σ_h‡. In particular, $h_i = 0$, $i > 0$ (respectively $i = 0$) implies that the orbit belongs to the stable (respectively unstable) boundary of S after the $(i-1)$th crossing (resp. before the 0th crossing). Using this interpretation, we assert that ℓ is given by the minimal integer j for which there exists a solution (h_0, t_0) to the equations†

$$\begin{aligned} &h_0 = 0 \qquad h_1 < 0 \qquad h_2 = 0 \\ &0 \leqslant \tau_0 \leqslant \frac{2\pi}{\omega} \qquad (j+\delta(\omega))\frac{2\pi}{\omega} \leqslant \tau_1 \leqslant (j+1+\delta(\omega))\frac{2\pi}{\omega} \\ &\delta(\omega) = \begin{cases} 1 & \text{if } \omega < 1 \\ 0 & \text{if } \omega > 1. \end{cases} \end{aligned} \tag{4.3}$$

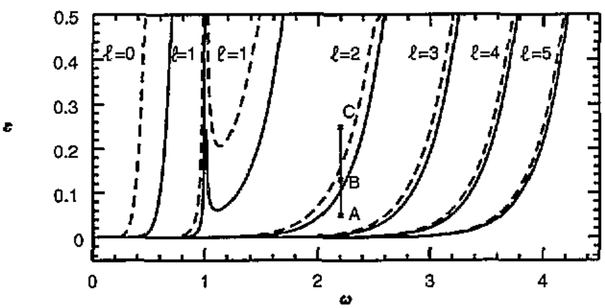

Figure 5. The topological bifurcation diagram. ——, $\epsilon_\ell^b(\omega)$; – – –, $\epsilon_\ell^a(\omega)$. ℓ values are indicated to the left of the curves.

Using the WM to approximate the h_i's and t_i's in (4.3), we found two families of solutions ('a,b'), each containing two solutions for $\epsilon > \epsilon_\ell^{a,b}(\omega)$, and none below these bifurcation values (see appendix B for details). In figure 5 we plot the bifurcation curves, which divide the parameter space to regions by the index ℓ, one of the flow transport order parameters.

As one increases ϵ along the line ABC in figure 5, the number of solutions to (4.3) changes, and therefore the structure of the manifolds of (2.2) changes, as shown in figure 6; for example, when $\epsilon_2^b < \epsilon < \epsilon_2^a$ (point B in figure 5), (4.3) has exactly two solutions with $j = 2$, and we estimate the structure index ℓ of (2.2) to be 2. Here, the tip of E_2 crosses $L(D_0)$, two homoclinic points in $E_2 \cap D_0$ are created (figure 6B), and the tangle has the same initial development as a type-2 trellis. A small increase (respectively decrease) in ϵ results in type-$(2, m, m, 0)$ trellises (respectively type-$(2, s, s, -1)$ trellises). In appendix A we

‡ We have recently proven that this argument may be made rigorous, e.g. that h_1 and h_2 can be made continuous by defining $h_i = 0$ on the boundary of S [25].

† In (3.8) of Rom-Kedar [32] we missed the index by one. This error was propagated through (3.12) and altered figures 5, 9 and 10. A similar error was made in (3.13a) of that paper, altering the indices in (3.14)–(3.17) and figure 7.

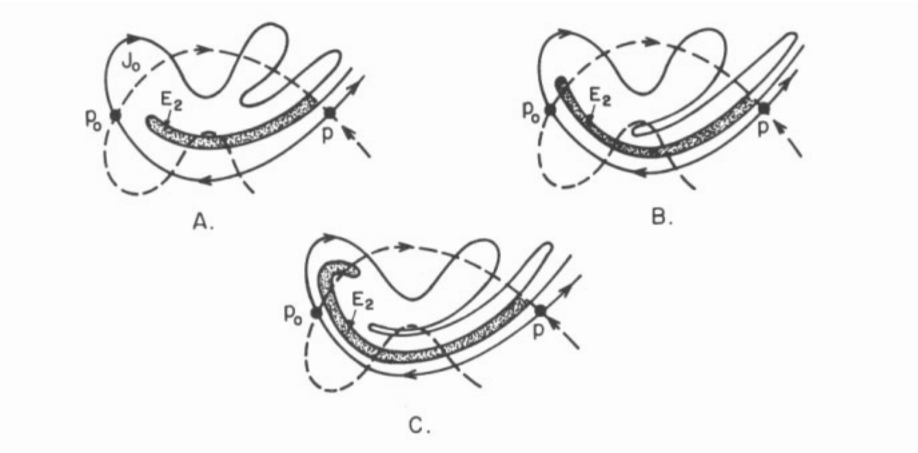

Figure 6. Geometrical interpretation of the bifurcation curves ϵ_ℓ^a and ϵ_ℓ^b. A: $\epsilon_3^a < \epsilon < \epsilon_2^b$; B: $\epsilon_2^b < \epsilon < \epsilon_2^a$; C: $\epsilon_2^a < \epsilon < \epsilon_1^b$.

(with Dana Hobson) compare the bifurcation diagram with a numerical bifurcation diagram, found by integrating the manifolds and searching for homoclinic tangencies. Figures A1 and A2 of the appendix are the numerical analogues to figures 6 and 5, respectively.

We found regions in parameter space in which the tangles had the same initial development as a type-ℓ trellis. In these regions the *finite time* topological and metric properties of the flow may be approximated using the properties of the simplest construction, the type-ℓ trellises. We extend our prediction to the asymptotic behaviour as well. As Robert MacKay remarked (private communication), when $\ell = 1$ we have some theoretical justification for this procedure; the horseshoe map, which is structurally stable, defines a type-1 trellis. Hence, we expect to find an open interval, contained in $[\epsilon_1^a, \epsilon_1^b]$, for which the map F is topologically conjugate to the horseshoe map and its manifolds form a type-1 trellis. Davis *et al* [29] find numerical evidence suggesting that the $(1, s, u, -1)$ trellises are structurally stable as well.

In the regions where the initial development of the tangles differs from that of a type-ℓ trellis, we need information regarding the fate of the tip of E_ℓ. This information is supplied by calculating the structure indices m, k. Recall that by symmetry, $m = k$ for (2.2). Following the arguments which led to (4.3), we find that an orbit contained in $L(E_\ell) \cap L(D_{-j})$ must satisfy:

$$\begin{gathered} h_0 = 0 \qquad h_1 < 0 \qquad h_2 < 0 \qquad h_3 = 0 \qquad 0 \leqslant \tau_0 \leqslant \frac{2\pi}{\omega} \\ (\ell + \delta(\omega))\frac{2\pi}{\omega} \leqslant \tau_1 \leqslant (\ell + 1 + \delta(\omega))\frac{2\pi}{\omega} \\ (j + \ell + \delta(\omega))\frac{2\pi}{\omega} \leqslant \tau_2 \leqslant (j + \ell + 1 + \delta(\omega))\frac{2\pi}{\omega}. \end{gathered} \tag{4.4a}$$

In addition, we demand that the orbit belongs to the tip of E_ℓ, therefore

$$\tau_0^2(\ell) \leqslant \tau_0 \leqslant \tau_0^3(\ell) \tag{4.4b}$$

where $\tau_0^2(\ell)$, $\tau_0^3(\ell)$ are the two interior solutions of (4.3) with $j = \ell$.

m is given by the minimal value of j for which there exists an initial condition (h_0, τ_0) which solves (4.4). These conditions are meaningful only in the regions where the tip is well defined, namely for $\epsilon_\ell^a < \epsilon$. equation (4.4) results in a nonlinear equation for $\tau_0(\epsilon, \omega; \ell)$. To find a bifurcation value one adds the requirement of vanishing derivative $(\mathrm{d}h_3/\mathrm{d}\tau_0 = 0)$ and obtains two nonlinear equations in the two unknowns (ϵ, τ_0), which can be solved numerically. Technically, it is quite difficult because the solutions τ_0 approach $\tau_0^2(\ell)$ or $\tau_0^3(\ell)$ exponentially in m. Indeed, we could not obtain reliable results for general m.

When $m = \ell$ or $m = \ell - 1$, we use the symmetry of our system to simplify the above equations. This reduces the number of unknowns by one, and enables us to calculate the bifurcation curves easily (see appendix B for details). The bifurcation curves $\epsilon_{\ell,m,m,0}^{a,b}$ of (4.4) for $m > l$ lie between ϵ_ℓ^a and $\epsilon_{\ell,\ell,\ell,0}^b$. The bifurcation curves $\epsilon_{\ell-1,m,m,-1}^{a,b}$ for $m \geqslant l$ lie between $\epsilon_{\ell,\ell-1,\ell-1,0}^b = \epsilon_{\ell-1,\ell-1,\ell-1,-1}^b$ and $\epsilon_{\ell-1}^b$. Hence, these two curves can be thought of as bounding the region in which the index m describes the tangle. We add the bifurcation curves $\epsilon_{\ell,\ell,\ell,0}^b$ and $\epsilon_{\ell-1,\ell-1,\ell-1,-1}^b$ to the ℓ bifurcation curves in figure 7. We observe that there are still large gaps between $\epsilon_{\ell-1,\ell-1,\ell-1,-1}^b$ and $\epsilon_{\ell,\ell,\ell,0}^b$; the implications of this observation will be discussed in section 5 (the curve $\epsilon_{\ell,\ell,\ell,0}^a$ lies between these two curves and is not shown).

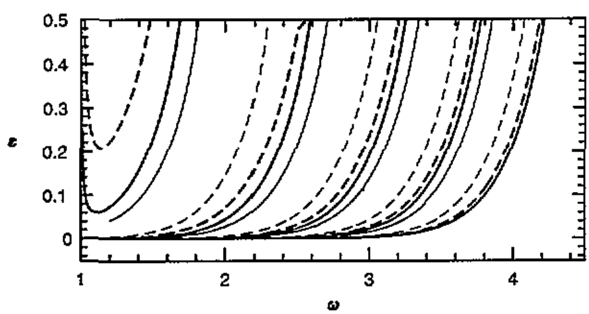

Figure 7. The m-bifurcation curves. On top of figure 5 we add: ---, $\epsilon_{\ell,\ell,\ell,0}^b$ and ——, $\epsilon_{\ell,\ell-1,\ell-1,0}^b$.

Close to the bifurcation curves $\epsilon = \epsilon_\ell^a$ the tip of E_ℓ is small, therefore we linearize the solutions of (4.4) about $\tau_0^2(\ell)$ and $\tau_0^3(\ell)$. Using the AWM, we find the approximate dependence of m on ϵ (see appendix B):

$$
\begin{aligned}
m^a &\approx \left[-\frac{3\omega}{4\pi}\log(|C(\omega)|(\epsilon - \epsilon_\ell^a)) - \frac{\omega}{2\pi}\log\frac{\omega}{648} - \frac{1}{2}\ell\right] \\
m^b &\approx \left[-\frac{3\omega}{4\pi}\log(|C(\omega)|(\epsilon - \epsilon_\ell^a)) - \frac{\omega}{2\pi}\log\frac{\omega}{648} - \frac{1}{2}\ell - \frac{1}{2}\right]
\end{aligned}
\tag{4.5}
$$

where $[x]$ denotes the integer part of x. It follows that the bifurcation curves $\epsilon_{\ell,m}^a$ and $\epsilon_{\ell,m}^b$ are exponentially close in m to ϵ_ℓ^a. (4.5) gives a perturbative estimate of the topology near the bifurcation. Generalizing m to a continuous variable enables one to estimate a topological critical index, as discussed in section 5.

5. Elongation rates of type-ℓ trellises

We summarize some of the methods developed by Rom-Kedar [22] for estimating the development of a type-ℓ trellis and then use this construction to estimate the exponential growth rate of segments of the unstable manifold. We conclude the section with a definition and an estimate of the transient time scale.

5.1. The structure of a type-ℓ trellis

The assumption that a type-ℓ trellis does not develop any spontaneous homoclinic points enables us to construct a one-sided symbolic dynamics which describes the dynamics of the lobes: we divide the tangled image of E_0 into several types of strips, called states. By the TAM assumptions, these states obey simple dynamical rules under the Poincaré map F. We draw typical members of the various states in figure 8 and define them as follows: the strips of $E_n \cap S$ which have one boundary belonging to $L(D_0)$ and another belonging to $L(D_j)$, $j \geqslant \ell$, belong to the state f_1. The strips of $E_n \cap S$ with one boundary belonging to $L(D_{-k})$ and the other belonging to $L(D_{\ell-k})$ or $L(D_{\ell-k+1})$, where $1 \leqslant k \leqslant \ell - 1$, belong to the state f_{k+1}. The strips of $F^n(E_0) \cap S$ which have one boundary belonging to $L(D_0)$ and another belonging to $L(D_1)$, belong to the state $f_{\ell+1}$. Finally, the arcs of $E_n \cap D_{-k}$, $k = 0, \ldots, \ell - 1$ belong, respectively, to the state g_k, $k = 1, \ldots, \ell$. The arcs of $E_n \cap D_j$, $j \geqslant 1$, belong to the state g_0.

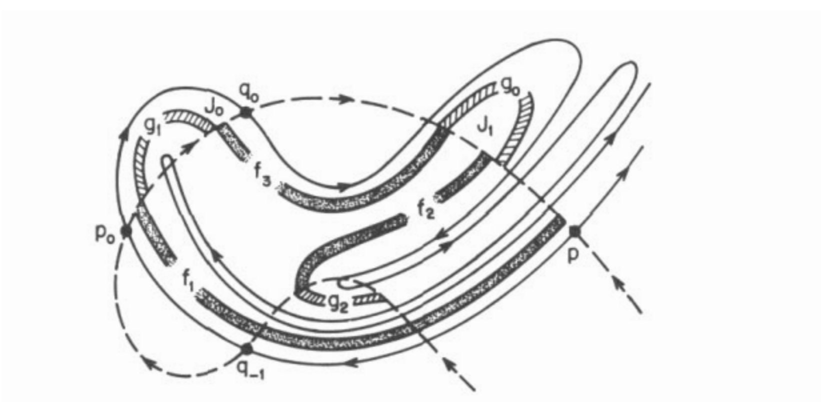

Figure 8. The states of a type-2 trellis. The hatched strips are the members of the indicated states.

By preservation of ordering along the stable and unstable manifolds and by their invariance, the states obey the following dynamics:

$$\begin{array}{l} \quad\ \nearrow\ f_1 \\ f_1 \longrightarrow f_{\ell+1} \Longrightarrow f_\ell \longrightarrow f_{\ell-1} \longrightarrow \cdots \longrightarrow f_1 \\ \quad\ \searrow\ g_1 \quad \searrow\ g_\ell \longrightarrow g_{\ell-1} \longrightarrow \cdots \longrightarrow g_1 \longrightarrow g_0 \end{array} \tag{5.1}$$

where '$f_{\ell+1} \Longrightarrow f_\ell$' means that one strip of type $f_{\ell+1}$ produces two strips of type f_ℓ. The dynamics of the states f_i determines the folding of curves inside S. In this section we may ignore the 'passive' states g_i and the width of the states f_i; both were introduced for the estimates of the escape rates (see section 6). From (5.1) we construct the $(\ell+1)\times(\ell+1)$ transfer matrix, T_ℓ:

$$T_\ell = \begin{pmatrix} 1 & 0 & 0 & \dots & 0 & 0 & 1 \\ 1 & 0 & 0 & \dots & 0 & 0 & 0 \\ 0 & 1 & 0 & \dots & 0 & 0 & 0 \\ 0 & 0 & 1 & \dots & 0 & 0 & 0 \\ \vdots & \vdots & \vdots & \ddots & \vdots & \vdots & \vdots \\ 0 & 0 & 0 & \dots & 1 & 0 & 0 \\ 0 & 0 & 0 & \dots & 0 & 2 & 0 \end{pmatrix}.$$

The number of strips of E_n ($n > 0$) belonging to a state f_i is bounded from below by the ith component of the vector $(0,\dots,0,1,0)\ T_\ell^{n-1}$: spontaneous intersections may only increase the number of strips. This observation enables us to estimate the length of $L(E_n \cap S)$:

$$L(E_n \cap S) \geqslant (0,\dots,0,1,0)\ T_\ell^{n-1}\Lambda \tag{5.2}$$

where Λ is a vector of lower bounds on the lengths of the states f_i. The exponential growth rate of these quantities is given by $\log \lambda_{T_\ell}$, where λ_{T_ℓ} denotes the modulus of the the largest root of the characteristic polynomial of T_ℓ,

$$p_\ell(\lambda) = \lambda^{\ell+1} - \lambda^\ell - 2 \qquad \ell \geqslant 2. \tag{5.3}$$

When $\ell = 1$, the matrix T_ℓ is replaced by the matrix

$$T_1 = \begin{pmatrix} 1 & 1 \\ 1 & 1 \end{pmatrix}$$

and $\lambda_{T_1} = 2$. In general, λ_{T_ℓ} is monotonically decreasing with ℓ (see table 1).

Table 1. Topological entropy and transient time of T_ℓ.

l	λ_0	λ_1	$U_{\text{trans}} = \log(10.0)/\log(\lambda_0/\lambda_1)$
1	2.000 000 0	1.000 000 0	3.321 928 1
2	1.695 620 8	1.086 052 0	5.168 543 8
3	1.543 689 0	1.138 243 3	7.557 166 8
4	1.451 085 1	1.157 918 0	10.202 510 6
5	1.388 093 5	1.163 364 6	13.037 323 4
6	1.342 152 2	1.162 542 0	16.027 405 0
7	1.306 990 0	1.158 923 6	19.150 690 5
8	1.279 108 0	1.154 109 7	22.391 337 1
9	1.256 391 8	1.148 870 1	25.737 259 2
10	1.237 483 9	1.143 584 3	29.178 864 3

5.2. The elongation rate of the unstable manifold

The bifurcation diagrams of figures 5 and 7 may be considered as an approximate diagram of the level sets of the topological entropy; if the type-ℓ trellises are similar to the tangles with the same initial development, then, for $\epsilon_\ell^b < \epsilon < \epsilon_\ell^a$, the exponential growth rate of line elements in phase space is given approximately by $\log \lambda_{T_\ell}$. A previous result along these lines has been obtained by Judd [20], who constructed a diagram describing the change in the topological entropy of the Duffing equation as the dissipation varies, using directed graphs to describe the evolution of the lobes and rough estimates, using the Melnikov function, to estimate the indices.

In Rom-Kedar [22], we constructed the symbolic dynamics for a type-$(\ell, m, k, 0)$ trellis for $m > l$ and calculated its eigenvalues. In table 2 we quote the values of λ_{T_ℓ} and $\lambda_{T_{\ell,m,m,0}}$ for several values of ℓ and m. Using the same approach, we construct the symbolic dynamics for $(\ell, m, m, 0)$ when $m = \ell, \ell - 1$ and find $\lambda_{T_{\ell,\ell,\ell,0}}$ and $\lambda_{T_{\ell,\ell-1,\ell-1,0}} = \lambda_{T_{\ell-1,\ell-1,\ell-1,-1}}$, which are quoted in the table as well. Comparing the differences in the topological entropies between the different families we notice that the 'central difference', $\lambda_{T_{\ell-1,\ell-1,\ell-1,-1}} - \lambda_{T_{\ell,\ell,\ell,0}}$ is smaller than the two 'side differences', $\lambda_{T_{\ell,\ell,\ell,0}} - \lambda_{T_\ell}$ and $\lambda_{T_{\ell-1}} - \lambda_{T_{\ell-1,\ell-1,\ell-1,-1}}$, and that the ratio between these differences increases with ℓ. We conclude that the critical increase in the topological entropy starts when the tips of the lobes $E_{\ell-1}$ and $D_{-\ell+1}$ intersect (type-$(\ell, \ell, \ell, -1)$ trellis), increases as m is varied and ends after they go through each other once more as a type-$(\ell, \ell, \ell, 0)$ trellis. The above observations were motivated by the derivation of Cammasa and Hobson using difference equations on lobe evolution, indicating that $(\ell, \ell, \ell, -1)$ is the 'critical bifurcation' (private communication). Figure 7 shows that there is a considerable gap between the curves $\epsilon^b_{\ell,\ell,\ell,0}$ and $\epsilon^b_{\ell-1,\ell-1,\ell-1,-1}$, and from table 2 we find that the topological entropies of these two tangles are almost the same. This implies that either there is no significant change in the dynamics in the gap, or that the topological entropy is not monotonic there. If the first possibility is occurring, then, perhaps the type-$(\ell, \ell, \ell, 0)$ trellis is structurally stable. Both possibilities are quite fascinating. The tools developed here, in Rom-Kedar [22] and in Davis *et al* [29] may be used to study this question.

Table 2. Topological entropy and transient time of type-(l, m, m, x) trellises.

l	m	x	λ	T_{trans}	l	m	x	λ	T_{trans}
1	1	0	2.269 53	18	6	6	0	1.362 13	85
1	5	0	2.001 99	29	6	0	0	1.342 15	91
1	0	0	2.000 00	23	6	6	−1	1.327 42	79
1	1	−1	1.891 10	28	7	7	0	1.322 53	103
2	2	0	1.803 70	28	7	0	0	1.306 99	108
2	5	0	1.703 25	36	7	7	−1	1.295 14	99
2	10	0	1.695 65	51	8	8	0	1.291 59	121
2	0	0	1.695 62	32	8	0	0	1.279 10	124
2	2	−1	1.638 41	38	8	8	−1	1.269 33	121
3	3	0	1.603 17	41	9	9	0	1.266 66	141
3	0	0	1.543 68	42	9	0	0	1.256 39	143
3	3	−1	1.507 46	47	9	9	−1	1.248 17	140
4	4	0	1.489 25	52	10	10	0	1.246 10	156
4	0	0	1.451 08	55	10	15	0	1.238 76	158
4	4	−1	1.425 72	56	10	20	0	1.237 63	169
5	5	0	1.414 89	68	10	0	0	1.237 48	163
5	0	0	1.388 09	72	10	10	−1	1.230 46	156
5	5	−1	1.369 18	65					

Using a least square fit for $\lambda_{T_{\ell,m,m,0}} - \lambda_{T_\ell}$ we have found [22] that for $m > l$:

$$\begin{aligned} \lambda_{T_{\ell,m,m,0}} &\approx \lambda_{T_\ell} + c_\ell \exp\{-2b_\ell m\} \\ b_\ell &\approx 0.68 - \tfrac{1}{4}\log\ell + 0.011\ell + \cdots . \end{aligned} \tag{5.4}$$

Using (4.5) and (5.4) we conclude:

$$\begin{aligned} \lambda_{T_{\ell,m,m,0}} - \lambda_{T_\ell} &\approx c_\ell \exp\{-2b_\ell m^a\} \\ &\approx c_\ell \exp(b_\ell l) \left(\frac{\omega}{648}\right)^{\frac{\omega b_\ell}{\pi}} [|C(\omega)|(\epsilon^a_{\ell,m} - \epsilon^a_\ell)]^{\frac{3\omega b_\ell}{2\pi}}. \end{aligned} \tag{5.5}$$

According to our construction, the topological entropy has plateaux which shrink exponentially with m, and their overall behaviour is described by (5.5). Smoothing out these plateaux we obtain a 'topological phase transition' with a critical index given approximately by:

$$\alpha_\ell = \frac{3\omega}{2\pi} b_\ell = \frac{3\omega(0.68 - \frac{1}{4}\log\ell + 0.011\ell + \ldots)}{2\pi}. \tag{5.6}$$

The first factor of the critical index, b_ℓ, is universal as it depends only on the geometry. The second factor $3\omega/2\pi$ is problem-dependent and is determined by the asymptotic behaviour of the period near the separatrix and by the form of the Melnikov function. According to the TAM approximation, the entropy is constant for $\epsilon^b_\ell < \epsilon < \epsilon^a_\ell$ and hence we conjecture that the topological entropy is not a smooth function in ϵ. To establish this conjecture one needs to prove that the lower bound on the topological entropy is realized on the plateaux, i.e. that the trellis is structurally stable there, as conjectured for the $(l, s, u, -1)$ trellises [29]. Another approach may be to add the additional structure of the trellis when the curve $\epsilon = \epsilon^a_\ell$ is approached from below (along the plateaux) and obtain a different rate of convergence. We may repeat the same process near each of the exponentially small plateaux by adding more indices and obtain pathological behaviour of the entropy—a Devil's Staircase. Troll [7] observed such behaviour in the family of truncated sawtooth maps: a hyperbolic, discontinuous, open family of mappings.

5.3. *The transient time*

In table 2 we include the transient time, the number of iterations we need until we achieve the convergence criteria of, say, a power method, to a given accuracy, $Error$ ($Error = 1.E-6$ for table 2). If λ_1 is the second largest root in magnitude, the convergence condition of the power method implies that:

$$T_{\mathrm{trans}} = \frac{|\ln(Error)| + C}{\ln\frac{\lambda_0}{\lambda_1}} \tag{5.7}$$

where $C = O(1)$ depends on λ_1, λ_0 and the initial vector one chooses for the matrix multiplications in the power method. An improvement of one digit in the estimate of λ_0 requires U_{trans} iterates of the matrix, where

$$U_{\mathrm{trans}} = \ln 10/\ln\frac{\lambda_0}{\lambda_1}. \tag{5.8}$$

In table 1 we list the *transient time unit* U_{trans} for the type-ℓ trellises. Comparing U_{trans} and T_{trans} of tables 1 and 2, we observe that $C = O(1)$ and has a non-monotonic dependence on ℓ. We also verify that changing the initial vector hardly changes T_{trans} (hence C), as is expected for a 'generic' choice of an initial vector.

Using a least square fit for $2 < \ell < 24$ we find

$$U_{\text{trans}}(\ell) \approx 1.98\ell^{1.175}. \tag{5.9}$$

Namely, U_{trans} grows faster than linear (the expected growth rate) with ℓ. The intuitive view that the ℓth power of the type-ℓ trellis behaves like a type-1 trellis is diminished by this calculation. Using the characteristic polynomial of the type-$(\ell,\ell,\ell,0)$ trellis:

$$P_{T_{\ell,\ell,\ell,0}} = (-1)^{\ell-1}\lambda^{\ell}(\lambda^{\ell+1} - \lambda^{\ell} - 2) + 2 \tag{5.10}$$

we find:

$$U_{\text{trans}}(\ell,\ell,\ell,0) \approx 1.78\ell^{1.2035}. \tag{5.11}$$

If the behaviour described by equations (5.9) and (5.11) is valid for $\ell \to \infty$, then, for $\ell > 70$ the transient time of the type-$(\ell,\ell,\ell,0)$ trellis will be larger than that of the type-ℓ trellis, i.e. we will have a non-monotonic dependence of U_{trans} on the indices.

6. The escape rates of type-ℓ trellises

6.1. *The semi-linear approximation*

We add a semi-linear approximation to the topological approximation by assigning weights to the dynamics described in (5.1). Then, we construct a weighted transition matrix, M_ℓ, which approximates the action of the flow on the states. Constructing an initial distribution vector for E_0, we estimate E_n distribution between the states by matrix multiplication. In particular, $e_n = \mu(E_n \cap D_0)$ is given by the 'mass' of E_n concentrated in the state g_1.

By construction, there are three non-trivial ($\neq 0$ or 1) weights, denoted by s_1, s_2 and s_3. s_1 (resp. s_2) measures the fraction of the area of a strip belonging to the state f_1 which maps to a strip belonging to the state f_1 (resp. $f_{\ell+1}$). s_3 measures the fraction of a strip belonging to $f_{\ell+1}$ which ends up as a strip belonging to the state f_ℓ. The weighted transition matrix is of the form:

$$M_\ell = \begin{array}{c} \begin{array}{cc} g_0\cdots g_\ell & f_1\cdots f_{\ell+1} \end{array} \\ \begin{pmatrix} L_{\ell+1} & 0 \\ R & W_\ell \end{pmatrix} \end{array}. \tag{6.1a}$$

The matrix W_ℓ realizes the dynamics on the f_i states:

$$W_\ell = \begin{pmatrix} s_1 & 0 & 0 & \dots & 0 & 0 & s_2 \\ 1 & 0 & 0 & \dots & 0 & 0 & 0 \\ 0 & 1 & 0 & \dots & 0 & 0 & 0 \\ 0 & 0 & 1 & \dots & 0 & 0 & 0 \\ \vdots & \vdots & \vdots & \ddots & \vdots & \vdots & \vdots \\ 0 & 0 & 0 & \dots & 1 & 0 & 0 \\ 0 & 0 & 0 & \dots & 0 & s_3 & 0 \end{pmatrix}. \tag{6.1b}$$

The matrix R administrates the transfer of areas from the f_i states to the g_i states:

$$R(1,2) = 1 - s_1 - s_2 \qquad R(\ell+1,\ell+1) = 1 - s_3 \qquad R(i,j) = 0 \text{ otherwise.} \tag{6.1c}$$

Finally, L_n is an $n \times n$ transfer matrix which reflects the trivial dynamics of the g_i states:

$$L_n = \begin{pmatrix} 1 & 0 & 0 & \dots & 0 & 0 & 0 \\ 1 & 0 & 0 & \dots & 0 & 0 & 0 \\ 0 & 1 & 0 & \dots & 0 & 0 & 0 \\ 0 & 0 & 1 & \dots & 0 & 0 & 0 \\ \vdots & \vdots & \vdots & \ddots & \vdots & \vdots & \vdots \\ 0 & 0 & 0 & \dots & 1 & 0 & 0 \\ 0 & 0 & 0 & \dots & 0 & 1 & 0 \end{pmatrix}. \tag{6.1d}$$

The lobe E_1 has, by construction, one part which belongs to an f_ℓ state and another small part which belongs to a g_ℓ state of area e_ℓ. Therefore, once $\mu(E_0)$, e_ℓ and the weights s_1, s_2 and s_3 are known, we can estimate e_n as the second component of the vector v^n:

$$e_n \approx v^n(2) = v^1 M^{n-1}(2) \tag{6.2}$$

where v^1 is a vector with $(2\ell + 2)$ components, two of which are non-vanishing:

$$v^1(\ell + 1) = e_\ell \qquad \text{and} \qquad v^1(2\ell + 1) = \mu(E_0) - e_\ell. \tag{6.3}$$

From the form of the matrix M_ℓ, it is easy to verify that the weights s_i can be estimated by:

$$s_1 \approx \frac{e_{\ell+2}}{e_{\ell+1}} \qquad s_2 \approx 1 - \frac{e_{\ell+1}}{\mu(E_0) - e_\ell} - \frac{e_{\ell+2}}{e_{\ell+1}} \qquad s_3 \approx 1 - \frac{e_{2\ell+1} - s_1^\ell e_{\ell+1}}{(\mu(E_0) - e_\ell)s_2}. \tag{6.4}$$

Therefore, given e_j, $j = \ell, \ell+1, \ell+2, 2\ell+1$ and $\mu(E_0)$, we can approximate the escape rates for all n. How should we determine the initial escape rates? In the next subsection we complete the theoretical prediction by estimating the escape rates using the WM. This gives an *a priori* estimate with no adjustable parameters (albeit with the possibility of improvement by refining the partition, as in Gaspard and Rice [8]).

6.2. Estimates of the initial escape rates

Since the variables (h, τ) of the separatrix map (4.1) are canonical variables, e_n is given by the integral of $\mathrm{d}h_0\mathrm{d}t_0$ evaluated between the values of (h_0, t_0) on the boundaries of the set $E_{-1} \cap D_{-n-1}$. Following Escande's ideas [3], we approximate these values using the WM (4.2), and derive the 'approximate action formula' to estimate these integrals (the derivation is included in appendix C): Let $t_i^a, t_i^b, h_i^a, h_i^b$ denote the crossing times and energies of two homoclinic orbits of order n (so $h_0^{a,b} = h_n^{a,b} = 0$), which are connected to each other by segments of stable and unstable manifolds, enclosing a simply connected domain (i.e. there are no additional homoclinic points of order $\leqslant n$ on the connecting segments). Let $t_0^a < t_0^b$. Then we conjecture that for sufficiently small ϵ and n, the area of this domain is given approximately by:

$$\int_{t_0^a}^{t_0^b} h_0(t_0)\,\mathrm{d}t_0 \approx -\epsilon \sum_{i=0}^{n} \int_{t_i^a}^{t_i^b} M(t)\,\mathrm{d}t - \sum_{i=1}^{n} \int_{h_i^a}^{h_i^b} hP'(h)\,\mathrm{d}h. \tag{6.5}$$

To evaluate e_j, $j = \ell, \ell + 1, \ell + 2, 2\ell + 1$ and $\mu(E_0)$, one needs to find the crossing times and energies of the relevant homoclinic points and their orderings (see appendix C).

Equation (6.5) is reminiscent of the formulae developed by MacKay *et al* [10] and by Bensimon and Kadanoff [33], expressing the area bounded by segments of the stable and unstable manifolds by differences in the actions of the homoclinic points. When $n = 0$, we obtain the well known result that the area of the lobe is given, to leading order in ϵ, by the integral of the Melnikov function [6, 34]. We conjecture that there exists an $\epsilon_0(N)$ such that for $\epsilon < \epsilon_0(N)$, (6.5) supplies the leading order approximation in ϵ for all $n < N$ to the exact formulae, given in terms of the differences in action of the homoclinic points. One could think of using the above formula for calculating the e_n's for all n's. However this is not a practical approach; the above formula requires a knowledge of all the homoclinic points of order n, t_i^k, and their ordering. Their number increases exponentially, and solving equations of the sort of (4.4) for higher iterates is non-trivial (MacKay *et al* [10] developed sophisticated numerical schemes for locating homoclinic orbits for twist maps); keeping track of the ordering after each iterate makes it even more difficult. Moreover, given an ϵ, the above formula will fail for sufficiently large n, and there are no *a priori* estimates for determining what is a 'large' n (see subsection 6.4).

6.3. *Discussion of the theoretical predictions and the limit $\epsilon \to 0$*

We calculated $\mu(E_0), e_\ell, e_{\ell+1}, e_{\ell+2}, e_{2\ell+1}$ for a 100 values of $\epsilon \in [\epsilon_\ell^b, \epsilon_\ell^a]$ and for several ω and ℓ values. Each computation, in which we solve the algebraic equations for the t_i's (the crossing times of the homoclinic points of order 2 and 3) for each $\epsilon \in [\epsilon_\ell^b, \epsilon_\ell^a]$ and calculate the integrals of (6.5) for $n \leqslant 3$, takes about 3 minutes of CPU time on a 20 MIPS DEC work station.

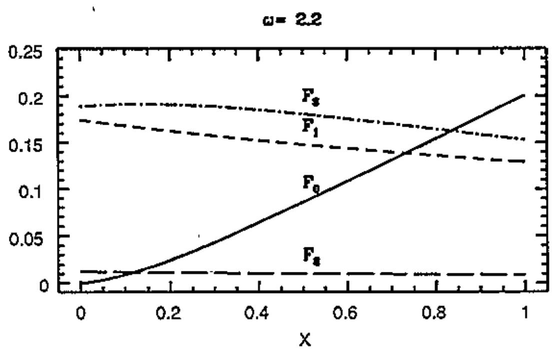

Figure 9. The self-similar escape rates. $F_i(X;\omega) = e_{j(i)}(\epsilon,\omega)/\mu(E_0(\epsilon,\omega))$ and $j(i) = \ell, \ell+1, \ell+2, 2\ell+1$ for $i = 0, \ldots, 3$.

The most striking finding is that the initial escape rates exhibit self-similar behaviour in ℓ. Fixing ω, we find that the dependence of the initial escape rates on ϵ is not trivial for $\epsilon_\ell^b < \epsilon < \epsilon_\ell^a$, yet this dependence is seemingly unchanged when $\epsilon_{\ell+1}^b < \epsilon < \epsilon_{\ell+1}^a$. This observation suggests that as $\epsilon \to 0$

$$\frac{e_{\ell+j}}{\mu(E_0)} = F_j(X, \omega) \qquad j = 0, 1, 2 \qquad \frac{e_{2\ell+1}}{\mu(E_0)} = F_3(X, \omega) \tag{6.6}$$

where

$$X = \frac{\epsilon - \epsilon_\ell^b}{\epsilon_\ell^a - \epsilon_\ell^b} \tag{6.7}$$

and the functions $F_i(X, \omega)$ are independent of ℓ or ϵ. In figure 9 we present these functions for $\omega = 2.2$. Note that the self-similarity is non-trivial: it involves rescaling in time as a function of ϵ (via ℓ) and focusing on special intersection sets. Since $\epsilon_\ell^a - \epsilon_\ell^b$ gets exponentially small in ℓ, we obtain a wild behaviour of the e_j's as functions of ϵ as $\epsilon \to 0$. The self-similarity of the e_j's may be caused by self-similarity of the solutions to equations (4.3) and (4.4): introducing the scaled variable X and using the AWM we found that the solutions to (4.3) are independent of ℓ and ϵ.

We found that the relative strength of $e_{2\ell+1}$ and $e_{\ell+1}$ changes with ω; for $1 < \omega < 2.4$, $\ell > 1$ we find that $e_{2\ell+1} > e_{\ell+1}$, and $e_{2\ell+1}$ is of the same order of magnitude as e_ℓ. As ω increases past the value 2.4 we find that $e_{\ell+1} > e_{2\ell+1}$. For large ω, both e_ℓ and $e_{2\ell+1}$ decrease, and $e_{\ell+1}$ and $e_{\ell+2}$ dominate. We notice that in all cases the contributions of the initial escape rates are significant, their sum varies between 30 and 40% of $\mu(E_0)$ for all the parameter values examined, and the relative weight of each of the initial escape rates varies with ϵ and ω. This finding strengthens our view that models which neglect this effect of correlation between entering and exiting lobes are bound to fail [16].

It follows from (6.6) and (6.4) that the weights governing the lobes dynamics, the s_i, exhibit a self-similar relation as well:

$$\frac{s_i - s_{i\,\min}}{s_{i\,\max} - s_{i\,\min}} = \tilde{F}_i(X, \omega) \qquad i = 1, 2, 3 \tag{6.8}$$

where $s_{i\,\min}$ and $s_{i\,\max}$ denote the minimal and maximal values of s_i in the interval $[\epsilon_\ell^b, \epsilon_\ell^a]$. In the limit $\epsilon \to 0$ these values should be fixed (independent of ℓ). In practice they change slightly with ℓ, whereas their difference is almost independent of ℓ. We also note that the overall change of s_i with ϵ is small yet not monotonic, on the order of 4% of its value as ϵ varies in the interval $[\epsilon_\ell^b, \epsilon_\ell^a]$. For $\omega \approx 2$ the weights obey $s_1 \ll s_3 \leqslant s_2$ (e.g. for $\omega = 2.084, \epsilon = 0.1$ we find $(s_1, s_2, s_3) = (0.055, 0.796, 0.723)$). As ω increases, s_2 decreases and s_1 and s_3 increase, so that when $\omega = 4.19$ we find $(s_1, s_2, s_3) = (0.308, 0.491, 0.903)$. The self-similarity and the asymptotic behaviour of the initial escape rates and weights for $\epsilon \to 0$ and $\omega \to \infty$, respectively, suggest that it is possible to find an analytic, asymptotic solution in these limits.

6.4. Asymptotic predictions and their relevance

According to the TAM, for any finite number of indices which are found for a tangle, the approximate e_n's decay exponentially as ζ^n, where ζ is the largest root of the characteristic polynomial of the weighted transition matrix. For the type-ℓ tangles, the characteristic polynomial is given by:

$$\zeta^{\ell+1} - s_1\zeta^\ell - s_2 s_3 = 0. \tag{6.9}$$

Given an ω and an ℓ we use (6.4) and (6.5) to calculate $\zeta_\ell(\epsilon, \omega)$ for $\epsilon \in [\epsilon_\ell^b, \epsilon_\ell^a]$. We observed that the decay rate is not necessarily monotonic in ϵ in each of these intervals, yet in general $\zeta \to 1$ as $\epsilon \to 0$. For example, fixing $\omega = 2.2$ and setting $\epsilon = 0.12, 0.0004$ (then $\ell = 2, 4$ respectively), gives $\ln\lambda = -0.165, -0.095$, respectively. Fixing ϵ and increasing ω makes λ increase, and changes the concavity of its graph (i.e. λ attains a maximum instead of a minimum in the interval $(\epsilon_\ell^b, \epsilon_\ell^a)$). When $\omega = 3.4$ the graph of λ is convex, and decreasing ϵ does not change the shape of the graph (namely, in this case the convexity is found in the self-similar regime). Incorporating the self-similar behaviour of the weights and the asymptotic dependence of ℓ on ϵ in (6.9), we obtain that as $\epsilon \to 0$, for some function G,

$$\zeta \approx 1 - \frac{1}{-\log\epsilon} G(\exp(-\mathrm{i}\log\epsilon)) + O\left(\frac{1}{(\log\epsilon)^2}\right).$$

In particular, we obtain that $\zeta \to 1$ logarithmically, with rapid oscillations as $\epsilon \to 0$. Recall that $e_n \propto e_N \zeta^{n-N}$ for large n and some $N \geqslant \ell$. Hence, for $\epsilon < 1$ we obtain that

$$e_n \propto e_N \exp\left(-\frac{n-N}{|\log\epsilon|} G(\exp(-\mathrm{i}\log\epsilon))\right) \tag{6.10}$$

and hence that $\sum_N^\infty e_n \propto e_N |\log\epsilon| / G(\exp(-\mathrm{i}\log\epsilon))$. For $N - \ell = O(1)$ we can establish that $e_N = o(\epsilon)$, hence, we obtain that $\sum_1^\infty e_n = \mu(E_0)$ converges as $\epsilon \to 0$ and the theory gives consistent results in this limit (notice that the summation and the limit $\epsilon \to 0$ are not interchangeable). Whether (6.10) really gives the asymptotic behaviour of the e_n's as $\epsilon \to 0$ is an open question.

Calculating the transient time unit U_{trans} (see (5.8)) for the escape rates, we found that U_{trans} is larger than the transient time units of the topological entropy by an order of magnitude (e.g. for $\omega = 2.2$, $\epsilon = 0.12$ we found $U_{\text{trans}}(\zeta) = 55$ whereas $U_{\text{trans}}(\lambda) = 5$). This implies that even for a tangle which satisfies all our topological and metric assumptions, a significant exponential decay will be seen only after a few hundred iterates. Moreover as ℓ increases U_{trans} is increased significantly. We notice that for all ω and ℓ values we chose, U_{trans} was found to be monotonically increasing with ϵ within each band, whereas decreasing ϵ and skipping to the next band by increasing ℓ, increased U_{trans}. In practice, we see the exponential decay quite early, but it is modulated by oscillations (see figure 10 below). These may be partly responsible for the large transient time unit we obtain, since they delay the convergence of the exponent.

We use the method developed in Rom-Kedar [22] to estimate the area of the invariant set. Denoting by $\tilde{M}_\ell$ the submatrix of M_ℓ (6.1) which does not include the state g_0 (crossing out the first row and column of M_ℓ) and by $\tilde{v}^1$ the vector v^1 (6.3) without its first component, we approximate the area of the invariant set by:

$$\begin{aligned} R_\infty \equiv \mu(Inv) &\approx \mu(S) - \mu(E_0)(1 + \delta(\omega)) - \sum_{s=2}^{2\ell+1} \tilde{v}^1 (I - \tilde{M}_\ell)^{-1}(s) \\ &\approx 1.2 - \mu(E_0)(2 - \delta(\omega)) + O(\epsilon^2) - \sum_{s=2}^{2\ell+1} \tilde{v}^1 (I - \tilde{M}_\ell)^{-1}(s) \end{aligned} \tag{6.11}$$

the first estimate involving the topological and semi-linear approximations. The second estimate (of $\mu(S)$) involves regular perturbation analysis—we estimate the difference in area enclosed by the perturbed and unperturbed orbits on a semi-infinite interval, following the same strategy as in the derivation of the Melnikov function. Using the calculations of the weights and of e_ℓ, we calculated R_∞ for several intervals of parameter values. We note that using (6.11) incorporates the exponential decay of the escape rates, yet overcomes the problem of long transient time predicted by U_{trans}. In all calculations we found that $\mu(R_\infty)$ is positive and monotonically decreasing with ϵ (e.g. for $\omega = 2.2$, $0.11 < \epsilon < 0.15$ we found $0.68 > \mu(R_\infty)/1.2 > 0.6$). A comparison of our predictions for the escape rates, e_n, with numerical experiments suggests (see next subsection) that at some point the rapid exponential decay of the escape rates relaxes to a slower decay rate. Therefore, our estimate of $\mu(R_\infty)$ is probably a lower bound on the area of the invariant set (see (3.1)).

Since hyperbolic and elliptic structures coexist near homoclinic tangles, it is controversial whether one should expect an exponential or a power law decay of the escape rates. In fact, Hillermeier *et al* [27] demonstrate that even a hyperbolic mapping (with symbolic dynamics consisting of a countably infinite number of symbols) may give rise to a power-law decay rate. Numerical experiments are not reliable for the long time evolution (notice that 'long time' is not well defined) and it is hard to prove that an approximate scheme (such as the TAM or the various Markov-chain models) gives the correct asymptotic behaviour in time. MacKay *et al* [10] argue that the stickiness of the cantori observed by Karney [35] should give a power law behaviour. As the model they presented gives an exponential decay, they postulated that refining their model to include an infinite number of states would result in a power law decay. For the TAM, any finite grammar classification of the tangle will give an exponential decay. Nonetheless, we may repeat their reasoning, and argue that refining our symbolic dynamics by including infinite number of indices will result in an infinite matrix hence, in a possible power-law decay rate. Hanson *et al* [36] used self-similarities of a discrete set of cantori approaching a boundary circle to construct an infinite-Markov-chain model which gives an algebraic decay rate of the survival probability. Meiss and Ott [14] incorporated the finer structures of the island chains and their cantori to construct an infinite-Markov-tree model to find a slower decay rate. As the referee noted, we may try and follow their ideas by incorporating self-similarities into the structure of the tangle to obtain algebraic decay. In any case, a solid conclusion on the asymptotic behaviour using methods like the TAM must be derived from investigation of the structural stability of the approximating trellises.

6.5. Comparison with numerical experiments and the WM

In figure 10 we present the computation of the e_n's using four different methods.

1. *A brute force method.* We find the boundaries of the lobe E_0 numerically, we distribute N initial conditions (typically $N \approx 40\,000$) on a regular grid in E_0 and integrate these initial conditions until they exit, recording the number of exiting particles in every Poincaré section. We use a fourth-order Adam–Moulton integrator (a predictor–corrector method). Typically, such a computation takes about 5 hours of CPU time on a 20 MIPS DEC workstation. While we do not expect our integration to be accurate per trajectory, the large amount of initial conditions and the concept of the shadowing lemma give us some confidence that our results regarding the escape rates are accurate. Indeed, increasing the number of initial conditions and decreasing the time step by a factor of two had only a small impact on the dips in the $\log e_n$'s oscillations for $n > 40$.

2. *The theoretical method.* We use (6.2) and (6.3) together with the approximate action formulae to compute the e_n's as described in subsections 6.1–6.3. This computation takes seconds of CPU time on the same workstation.

3. *The semi-theoretical method.* We use (6.2) and (6.3), but use the results of the brute force computations to obtain the values of the initial escape rates. We include this mix of methods because it isolates the topological and semi-linear approximations from the perturbation analysis. We found no significant difference between the semi-theoretical and theoretical predictions.

4. *The WM iterates.* We replace the dynamics of our system with the WM: we distribute N ($\approx 40\,000$) points evenly in the region $0 \leqslant t_0 \leqslant \pi/\omega$, $0 < h_0 < \epsilon M(t_0)$, and evolve each initial condition according to the WM (4.2). Once a particle escapes (has a positive energy),

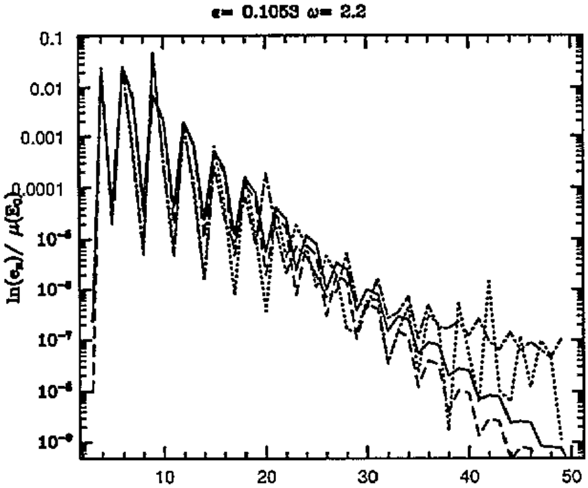

Figure 10. The escape rates—comparison. – – –, brute force computation; ——, theory; - - - -, semi-theoretical; — · —, WM computation.

the escape set with the corresponding exit time is increased by one. This computation takes about 5–10 minutes of CPU time.

We found satisfactory agreement between our predictions and the numerical calculations. Moreover, for some parameters, the theoretical prediction seemed to give the best overall fit to the numerical calculation. In table 3, we compare the series $x_n = \ln(e_n) - \ln(e_{n-1})$, $n \leqslant 40$ found by the last three methods to the numerical computations. We list the values of the χ^2-test, the correlation r and the ratio between the averages of x_n and the numerical average, which gives the exponential decay rate λ. This table quantifies what one observes from a sequence of figures like figure 10; that the theoretical prediction does pretty well for all parameter values, that in general it is better for smaller ϵ values, yet it performs better on the bifurcation curve ϵ_ℓ^a than slightly below it, and that it is more robust than the WM.

Table 3. Statistical comparison of the e_n's calculations.

Parameters				Theory			Semi-Theory			Whisker map		
ω	ε	X	l	χ^2	r	$\frac{\lambda}{\lambda_{num}}$	χ^2	r	$\frac{\lambda}{\lambda_{num}}$	χ^2	r	$\frac{\lambda}{\lambda_{num}}$
2.2	0.105	$\frac{1}{100}$	2	1.230	0.887	1.047	1.057	0.883	1.021	1.477	0.835	1.039
2.2	0.117	$\frac{1}{4}$	2	1.293	0.830	1.016	1.238	0.821	1.028	2.116	0.675	1.010
2.2	0.131	$\frac{1}{2}$	2	1.612	0.743	0.998	1.758	0.719	1.016	2.910	0.542	0.942
2.2	0.144	$\frac{3}{4}$	2	1.824	0.677	1.009	2.120	0.641	1.033	2.897	0.513	0.965
2.2	0.157	1	2	1.765	0.679	0.998	1.992	0.652	1.025	3.523	0.429	0.979
2.8	0.086	$\frac{1}{100}$	3	1.011	0.831	1.001	4.875	0.029	0.948	0.910	0.847	0.975
2.8	0.092	$\frac{1}{4}$	3	1.183	0.820	1.022	1.136	0.820	1.006	0.925	0.861	1.005
2.8	0.098	$\frac{1}{2}$	3	1.128	0.795	0.999	1.125	0.795	0.996	0.536	0.912	0.978
2.8	0.104	$\frac{3}{4}$	3	1.598	0.747	1.007	1.582	0.748	1.008	0.710	0.897	0.981
2.8	0.111	1	3	1.388	0.780	1.017	1.353	0.782	1.018	0.627	0.908	0.986

Examining figure 10, we observe three interesting phenomena: the oscillations of the e_n's for all n's, the exponential decay for $n < N_{\text{break}}$, and the sudden change from the exponential decay to a different regime for $n > N_{\mathrm{break}}$. Comparing the different curves we notice that for a few oscillation periods, the theoretical and numerical results follow closely. Then, at some point (denoted by N_{shift} in table 4), the real tangle encounters a tangency or an intersection which is not predicted by the topological approximation, and we get a shift in the e_n's. In table 4 we list the approximate value of N_{break}, found by inspection of figures such as figure 10. We include in the table the N_{shift} and N_{break} values of the WM simulation for comparison.

Table 4. Properties of the e_n's calculations.

Parameters				Numerical				Whisker map			
ω	ε	X	l	Period	Var	N_{shift}	N_{break}	Period	Var	N_{shift}	N_{break}
2.2	0.1053	0.01	2	2.889	0.457	22	36	2.833	0.500	19	30
2.2	0.1174	0.25	2	2.833	0.617	22	36	2.736	0.315	16	48
2.2	0.1306	0.50	2	2.684	0.228	19	36	2.550	0.260	13	38
2.2	0.1438	0.75	2	2.666	0.234	19	36	2.944	0.644	13	30
2.2	0.1571	1.00	2	2.684	0.228	16	40	2.550	0.260	13	30
2.8	0.0862	0.01	3	3.125	0.783	21	55	3.571	0.725	17	38
2.8	0.0920	0.25	3	3.333	0.952	17	50	3.846	0.641	17	45
2.8	0.0982	0.50	3	3.333	0.952	17	42	3.571	1.802	17	45
2.8	0.1044	0.75	3	3.400	0.543	17	35	3.571	0.879	17	35
2.8	0.1107	1.00	3	3.333	0.809	17	38	3.062	0.596	17	38

The theory predicts the period of the oscillations to be approximately $\ell + 1$ Poincaré periods for a type-ℓ trellis. The numerical results follow this trend. In table 4 we list the mean and variance of the distances between adjacent local maxima of the numerical e_n's, and the ones calculated with the WM for two values of ω and for several distances, X (see (6.6)), from the bifurcation curves. The averages are taken over 60 Poincaré periods. For $\ell = 2$ the averages are quite close to the predicted average of 3.0. However for $\ell = 3$, the averages of the numerical periods are much lower than the predicted period, 4.0 (most of the shorter oscillations seem to occur for intermediate times $-20 < n < 35$). The statistics of the WM oscillations seems to be different.

7. Discussion

We developed the TAM and used it to analyse the phase space flow of a particle in a cubic potential, perturbed by temporally periodic forcing. We summarize the TAM and our main results in table 5. This study demonstrates the usefulness and relevance of the TAM; we predict the transient behaviour of the system for a whole range of parameter values, based upon the underlying structures, using less than five minutes of workstation time (solving a few algebraic equations). Moreover, this approach seems to focus the study on the 'correct' quantities leading to the discovery of non-trivial self-similarities.

We found that the 'first-order' approximation of the tangles, by the type-ℓ trellises, fails to predict the long time ($e_n > e_{N_{\mathrm{break}}}$, $30 < N_{\mathrm{break}} < 50$) and asymptotic behaviour of the escape rates. We expect similar behaviour of the elongation rates. Taking better topological approximations (adding more indices) would improve the agreement between the model and the flow thereby increasing the value of N_{break}. However, it is unclear whether any finite grammar approximation of this sort could give the correct asymptotic behaviour for

Table 5. TAM—topological approximation method.

Concept	Motive	Tools	Assumptions	Remarks
Topological bifurcation diagram	classify tangle by indices	WM & structure indices definition	near-integrable system	can find numerically in the non-perturbative case
Manifold length				
(i) finite time estimates	interface length	symbolic dynamics for the lobes evolution	topological approximation: 'finite grammar'	application to chemically reacting fluids
(ii) asymptotics	lower bound on topological entropy	symbolic dynamics for the lobes eolution	topological approximation 'finite grammar'	gives 'topolological phasetransition'& indicative of 'Devil Staircase' for the topol. entropy
Transport rates				
(i) initial escape rates (i.e.r.)	initial conditions for the transport process	WM and the approximate action formula	near-integrable system	exhibit self-similarity as $\epsilon \to 0$
(ii) weighted symbolic dynamics	obtain estimates for the escape rates	i.e.r. $\to$ weights lobes symbolic dynamics	topolological approximation and semi-linear approximation	weights exhibit self-similarity as $\epsilon \to 0$
(iii) Escape rates				
(1) finite time	(1) transient behaviour	weighted symbolic dynamics	topological approximation and	(1) oscillatory behaviour
(2) asymptotic	(2) *find exponential* decay rate	*& weighted transition matrix*	*semi-linear approximation*	(2) *breaks down for* $n > N_{\text{break}}$
(3) transient time unit	(3) transient period			(3) gives long transient times
(iv) area of invariant set, R_∞		weighted symbolic dynamics & perturbation method	topological approximation and semi-linear approximation	expect $R_\infty > R_\infty$(theoretical)

some interval of parameter values—namely if the trellises are structurally stable. It might be necessary to include an explicit modelling of the influence of the elliptic structures on the homoclinic tangle.

We argued that by using the topological approximation tools, one can improve the approximation to higher accuracy. However, we do not supply any quantitative estimates for the 'accuracy' of our method. The topological and semi-linear approximations are based upon geometrical arguments and have no rigorous justifications or error estimates. Finding structurally stable maps which attain type-ℓ trellises would substantiate the validity of the TAM. If these do not exist, a consistent construction of trellises of countable infinity indices with converging properties to the type-ℓ trellises may be needed. Construction of the type-$(\ell, m, m, 0)$ trellises gives a good indication that such a convergence exists. This construction may be used to estimate the errors involved in the topological and semi-linear approximations. Recently [25], we have proven that the perturbation analysis we developed is valid in the limit $\epsilon \to 0^+$, and have supplied the corresponding error estimates for that part of the analysis.

Our results are valid for sufficiently small ϵ, and for finite values of ω which are bounded away from zero and one; for $\omega = 0, 1$ or infinity, the Melnikov function vanishes identically, and we cannot conclude upon the structure of the homoclinic tangle using the WM approximation. The limit $\omega \to 0$ is the adiabatic limit, in which the homoclinic tangle has large lobes [3, 37] ($\ell = 0$), hence different symbolic dynamics for the lobes needs to be developed. For $\omega \approx 1$, the structure of the tangle is determined by the next non-vanishing term in the expansion series of the distance function in ϵ, and the perturbation theory and its error estimates must be modified accordingly. In the limit $\omega \to \infty$ we expect to see exponentially small separation of the manifolds [38], hence a failure of our regular perturbation theory. Formally, this limit corresponds to $\ell \to \infty$ in our analysis, and we observed interesting trends of the escape rates and weights in this limit. The significance of the asymptotic behaviour of our model in this limit is an open question.

We demonstrated that the TAM can be used to obtain a global description of the changes in the properties of the flow as the parameters vary. Moreover, we found that these methods are easy to apply, require a negligible amount of numerical computations and programming, and supply a reasonable approximation of the brute force calculation. Therefore, we expect to see extensions of the TAM to closed flows [17], quasi-periodic flows and higher dimension Hamiltonian systems, at least for cases in which the additional dimensions do not change the geometry of the tangle too dramatically and can be viewed as small perturbations to the structures we have introduced. Other developments may be in the direction of incorporating cutoff scales to the system, to account for diffusivity of particles; since the TAM includes a detailed account of the width of the lobes at any given time, it seems like a natural framework for such a study. Using the TAM approach to construct a 'Devil's staircase' for the topological entropy [7, 29] and for constructing numerical schemes for computing the topological entropy also seems promising. Finally, allowing the perturbation to be slightly dissipative should not alter any major part of the TAM, and may shed some light on the issue of strange attractors, as these can be viewed as the limiting set of the lobes.

Acknowledgments

This work was started at the University of Chicago, continued during my visits to the Observatoire de Côte d'Azur, Nice and to the Equipe Turbulence Plasma of URA 773 CNRS-Université de Provence at Institut Méditerranéen de Technologie, Marseilles, and was completed at the Weizmann Institute in Israel. I take pleasure in thanking all the people who arranged these visits, and with whom I discussed this work as it developed: Leo Kadanoff from the University of Chicago, Pierre-Louis Sulem from the Observatoire and Yves Elskens and Dominique Escande from Turbulence Plasma. I also benefited from discussions with Robert MacKay. I thank Anna Litvak-Hinanzon for calculating the Melnikov integral. Finally, I thank Dana Hobson for his comments, and his agreement to include our common work in appendix A. The research described in this paper was partially supported by NSF grant DMS8903244, ONR grant N00014-90J1194, and by the ministry of Absorption of the State of Israel.

Appendix A. Numerical bifurcation diagram†

In figure 11 we present the numerical version of figure 5: We fix $\epsilon = 0.1$ and vary ω. For $\omega = 2.3, 2.2, 2.1$ and 1.9 the lobes E_1 and D_{-1} (hence E_2 and D_0) intersect each other in $0, 1, 2$ and 4 homoclinic points, respectively. These results are in good agreement with our theory which predicts, for $\epsilon = 0.1$ that the bifurcations will occur at $\omega = 2.189$ and 2.083 respectively. To obtain these diagrams we use the method and code developed by D Hobson [39] for accurate integration of the stable and unstable manifolds.

To obtain a numerical bifurcation diagram, we incorporate into Hobson's code conditions for tangencies. While general conditions for tangencies are quite complicated to program, the tangencies we are interested in can be found using the the symmetries of the manifolds in the symmetric Poincaré sections ($t_0 = 0, \pi/\omega$). Once the conditions are formulated, we use an arc length continuation scheme in ω and ϵ for finding the bifurcation curves.

First, note that given that lobes A and B are symmetric with respect to reflection about the x-axis, a tangent bifurcation of $A \cap B$ (and their images and pre-images) exists when A (hence B) is tangent to the x-axis. Similarly, the bifurcation from two to four intersection points of $A \cap B$ happens when the front part of A is perpendicular to the x-axis. Hence, once the appropriate lobes and Poincaré sections are defined, a continuation parameter for the bifurcation curve $\epsilon_\ell^a(\omega)$ is the distance of a symmetric lobe from the x-axis. Similarly, a continuation parameter for finding the bifurcation curves $\epsilon_\ell^b(\omega)$ is the angle between the tangent to a symmetric lobe at the front point of intersection and the x-axis. This observation implies that the symmetry forces the degenerate bifurcation of $\epsilon_\ell^b(\omega)$.

For our model, the following symmetries of the tangle hold:

1. When $\omega > 1$ (resp. $\omega < 1$) and ℓ is odd, letting $\ell = 2k+1$, the lobes E_k and D_{-k-1} are symmetric in the Poincaré map with the zero (respectively $\frac{\pi}{\omega}$) phase.

2. When $\omega > 1$ (resp. $\omega < 1$) and ℓ is even, letting $\ell = 2k$, the lobes E_k and D_{-k} are symmetric in the Poincaré map with the $-\frac{\pi}{\omega}$ (respectively zero) phase.

Using these symmetries in the Poincaré sections $0, \pi/\omega$, we find the bifurcation curves $\epsilon_\ell^a(\omega), \epsilon_\ell^b(\omega)$ for all ω, ℓ. We compare the numerical bifurcation curves and our analytical predictions in figure 12. We observe that for $\omega > 2$, the agreement is quite satisfactory even for large values of ϵ. For small values of ω we are approaching the adiabatic limit, and as expected, our analysis fails.

† This appendix by Dana Hobson and the author.

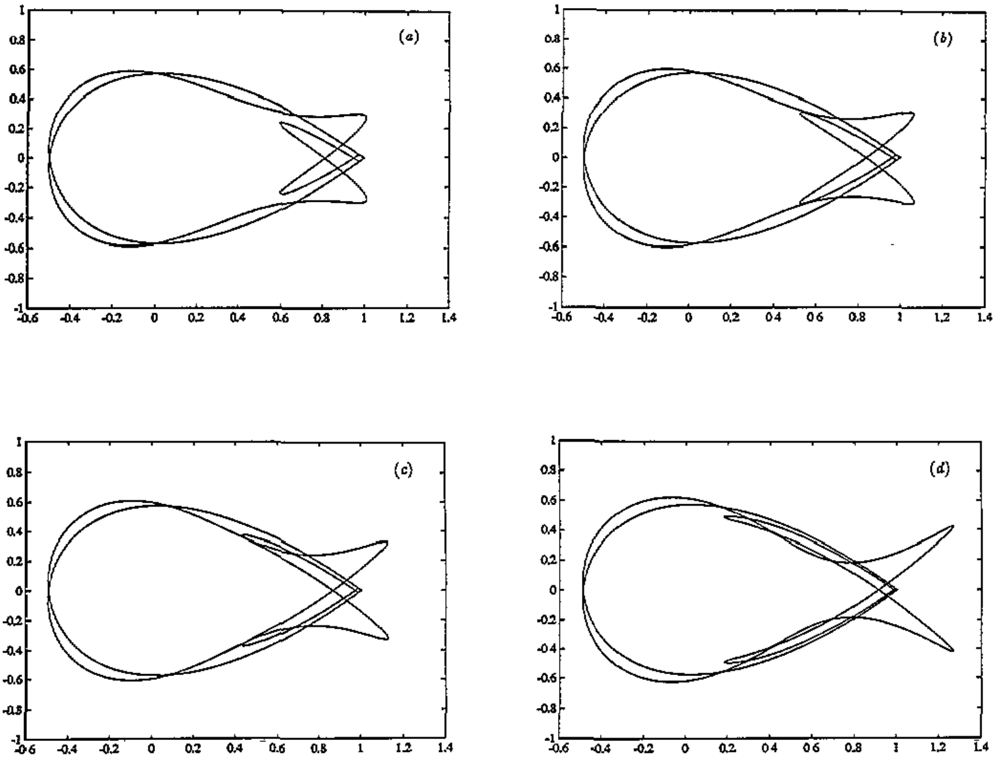

Figure A1. The geometrical interpretation of the bifurcation curves $\epsilon_\ell^a, \epsilon_\ell^b$. $\epsilon = 0.1$ in all figures. (*a*) $\omega = 2.3$, $\epsilon_3^a < 0.1 < \epsilon_2^a$; (*b*) $\omega = 2.2$, $\epsilon_2^b \approx 0.1$; (*c*) $\omega = 2.1$, $\epsilon_2^b < 0.1 < \epsilon_2^a$; (*d*) $\omega = 1.9$, $\epsilon_2^a < 0.1 < \epsilon_1^b$.

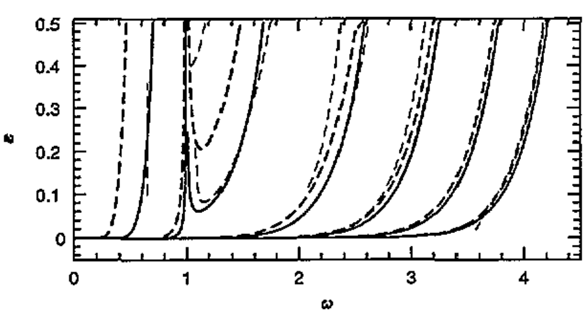

Figure A2. Numerical and analytical topological bifurcation diagram. – – –, numerical; ——, $\epsilon_\ell^b(\omega)$; - - - -, $\epsilon_\ell^a(\omega)$, analytical.

Appendix B. The bifurcation curves

B.1. The ℓ-bifurcation curves

Using (4.2), we find that (4.3) amounts to finding a solution $0 \leqslant \tau_0 \leqslant \frac{2\pi}{\omega}$ to:

$$\begin{aligned} &M(\tau_0) = -M(\tau_0 + P(\epsilon M(\tau_0))) \\ &(j+\delta(\omega))\frac{2\pi}{\omega} < P(\epsilon M(\tau_0)) + \tau_0 \leqslant (j+1+\delta(\omega))\frac{2\pi}{\omega}. \end{aligned} \tag{B.1}$$

The solutions of (B.1) satisfy:

$$\sin(\omega\tau_0^i) = \frac{1}{\epsilon C(\omega)} P^{-1}\left(\left(j+\frac{1}{2}\right)\frac{2\pi}{\omega}\right) \qquad i = 2, 4 \tag{B.2a}$$

or

$$\sin(\omega\tau_0^i) = \frac{1}{\epsilon C(\omega)} P^{-1}\left(-2\tau_0^i + (j+1+\delta(\omega))\frac{2\pi}{\omega}\right) \qquad i = 1, 3 \tag{B.2b}$$

where $\tau_0^i \in I_\omega$, $\tau_0^1 \leqslant \tau_0^2 \leqslant \tau_0^3 \leqslant \tau_0^4$, and

$$I_\omega = \begin{cases} [\pi/\omega, 2\pi/\omega] & \text{for } \omega < 1 \\ [0, \pi/\omega] & \text{for } \omega > 1. \end{cases}$$

We equate the right-hand side of (B.2a) to one, and find the bifurcation curves for (B.2a):

$$\epsilon_\ell^a = \frac{P^{-1}\left(\left(\ell+\frac{1}{2}\right)\frac{2\pi}{\omega}\right)}{|C(\omega)|} \approx \frac{72\exp\left(-\left(\ell+\frac{1}{2}\right)\frac{2\pi}{\omega}\right)}{|C(\omega)|}. \tag{B.3}$$

For $\epsilon < \epsilon_\ell^a$, (B.2$a$) has no solutions, and for $\epsilon \geqslant \epsilon_\ell^a$ (B.2a) has two solutions, $\tau_0^2(\ell) \leqslant \tau_0^4(\ell)$. The bifurcation curves $\epsilon_\ell^a(\omega)$, $0 \leqslant \ell \leqslant 5$ are plotted in figure 5 (the dashed lines). We obtain the bifurcation curves of (B.2b) by requiring the function

$$f(\tau_0) \equiv \epsilon\sin(\omega\tau_0) + \frac{P^{-1}\left(-2\tau_0 + (\ell+1+\delta(\omega))\frac{2\pi}{\omega}\right)}{C(\omega)} \tag{B.4}$$

to have a quadratic zero in the appropriate interval of τ_0. Eliminating ϵ, we obtain the following algebraic equation for τ_0:

$$\tan(\omega\tau_0) = -\frac{\omega}{2}h(\tau_0)\frac{\mathrm{d}P(h(\tau_0))}{\mathrm{d}h} \qquad h(\tau_0) \equiv P^{-1}\left(-2\tau_0 + (\ell+1+\delta(\omega))\frac{2\pi}{\omega}\right). \tag{B.5}$$

We use the AWM to obtain an initial guess for τ_0 at the bifurcation:

$$\tau_0^1(\ell) = \tau_0^3(\ell) \approx \frac{1}{\omega}\tan^{-1}\left(\frac{\omega}{2}\right). \tag{B.6}$$

Using this initial guess and a Newton method with an arc length continuation method we solve (B.5), substitute in (B.4) and obtain the bifurcation curves $\epsilon_\ell^b(\omega)$ of figure 5 (the solid lines). Using the AWM (2.5a) we estimate:

$$\epsilon_\ell^b \approx \frac{72}{|C(\omega)|}\frac{\sqrt{1+\frac{\omega^2}{4}}}{\frac{\omega}{2}}\exp\left(-(\ell+1+\delta(\omega))\frac{2\pi}{\omega} + \frac{2}{\omega}\tan^{-1}\left(\frac{\omega}{2}\right)\right) \tag{B.7}$$

where $\tan^{-1}(\frac{\omega}{2})$ is chosen to belong to I_ω. We note the peculiar property that, to leading order in ϵ, (4.3) has a degenerate bifurcation from two to four solutions. C Simô has remarked (private communication) that this degeneracy is a common feature in homoclinic tangles and it is associated with the symmetries of the homoclinic tangent bifurcation. In Appendix A we (with Dana Hobson) give a simple geometrical argument for this occurrence.

B.2. The m-bifurcation curves

Using (4.2), we find that (4.4) amounts to finding a solution τ_0 to:

$$\begin{aligned}
&\tau_1 = \tau_0 + P(\epsilon M(\tau_0))\\
&\tau_2 = \tau_1 + P(\epsilon M(\tau_0) + \epsilon M(\tau_1))\\
&h_3 = \epsilon(M(\tau_0) + M(\tau_1) + M(\tau_2)) = 0 \qquad\qquad (\text{B.8}a)\\
&(j + \ell + \delta(\omega))\frac{2\pi}{\omega} \leqslant \tau_1 + P(\epsilon M(\tau_0) + \epsilon M(\tau_1)) \leqslant (j + \ell + 1 + \delta(\omega))\frac{2\pi}{\omega}
\end{aligned}$$

with

$$\tau_0^2(\ell) \leqslant \tau_0 \leqslant \tau_0^3(\ell). \qquad (\text{B.8}b)$$

We solve (B.8) in two cases:

Case 1. When $m = \ell$ or $m = \ell - 1$, we use the symmetry of our system to simplify the above equations. By the symmetry of the tangle, one can show that the two symmetric solutions satisfy:

$$\begin{aligned}
\tau_1 &= \left(\ell + \frac{1}{2} + \frac{1}{2}\delta(\omega)\right)\frac{2\pi}{\omega} \qquad (\ell, \ell, \ell, 0) \text{ trellis}\\
\tau_1 &= \left(\ell + \frac{1}{2}\delta(\omega)\right)\frac{2\pi}{\omega} \qquad (\ell, \ell - 1, \ell - 1, 0) \text{ trellis.}
\end{aligned} \qquad (\text{B.9})$$

These identities allow us to eliminate ϵ from the bifurcation equation, and obtain the following equation for τ_0:

$$\tan(\omega\tau_0) = -\omega h(\tau_0)\frac{\mathrm{d}P(h(\tau_0))}{\mathrm{d}h} \qquad h(\tau_0) \equiv P^{-1}(\tau_1 - \tau_0) \qquad (\text{B.10})$$

which, together with (B.9), is of the same form as (B.5) and can be solved easily. $\epsilon^b_{\ell,\ell,\ell,0}$ and $\epsilon^b_{\ell,\ell-1,\ell-1,0}$ are then found from $\epsilon = \frac{P^{-1}(\tau_1 - \tau_0)}{M(\tau_0)}$.

Case 2. We estimate the solutions to (B.8) and exert their dependence on m near $\epsilon = \epsilon^a_\ell$. There, the tip of E_ℓ is small, therefore the distance between the zeros $\tau_0^2(\ell)$ and $\tau_0^3(\ell)$ is small. In fact, expanding (B.2) in $\bar{\epsilon} = \epsilon - \epsilon^a_\ell$ we find:

$$\begin{aligned}
\tau_0^2(\ell) &= \frac{\pi}{\omega}\left(\frac{1}{2} + \delta(\omega)\right) - \frac{1}{\omega}\sqrt{\frac{2\bar{\epsilon}}{\epsilon^a_\ell}} + O(\bar{\epsilon}^{3/2})\\
\tau_0^3(\ell) &= \frac{\pi}{\omega}\left(\frac{1}{2} + \delta(\omega)\right) + \frac{1}{2}\bar{\epsilon}|C(\omega)|P'(-\epsilon^a_\ell|C(\omega)|) + O(\bar{\epsilon}^2) \approx \frac{\pi}{\omega}\left(\frac{1}{2} + \delta(\omega)\right) + \frac{1}{2}\frac{\bar{\epsilon}}{\epsilon^a_\ell}
\end{aligned} \qquad (\text{B.11})$$

hence,

$$\tau_0^3(\ell) - \tau_0^2(\ell) = \frac{1}{2}\bar{\epsilon}|C(\omega)|P'(-\epsilon^a_\ell|C(\omega)|) + \frac{1}{\omega}\sqrt{\frac{2\bar{\epsilon}}{\epsilon^a_\ell}} + O(\bar{\epsilon}^{3/2}) \approx \frac{1}{\omega}\sqrt{\frac{2\bar{\epsilon}}{\epsilon^a_\ell}} + \frac{1}{2}\frac{\bar{\epsilon}}{\epsilon^a_\ell} + \cdots$$

where P' denotes the derivative of P w.r.t. the argument and the approximate sign is used when we replace the WM with the AWM (2.5a). This enables us to write explicit expressions in ϵ, yet the errors are expected to be much worse (the estimates involve terms multiplying $\log(\epsilon)$, and were omitted). Define the tip variable, θ^i, by

$$t_0^i = \tau_0^i(\ell) + \theta^i \qquad i = 2, 3 \qquad \text{and} \qquad \theta^2 > 0, \theta^3 < 0. \tag{B.12}$$

Assuming $|\theta^i| \ll 1$, linearizing (B.8) about $\tau_0^i \equiv \tau_0^i(\ell), i = 2, 3$ and using (B.1) and (B.11) we find after some algebra that:

$$\begin{aligned} \theta_\pm^2 &\approx \frac{36}{\bar\epsilon |C(\omega)|\omega^2} \exp\left(-j \pm 1/4 - \frac{1}{\omega}\sqrt{\frac{2\bar\epsilon}{\epsilon_\ell^a}}\right) \\ \theta_\pm^3 &\approx -\frac{72}{\bar\epsilon |C(\omega)|\omega^2} \exp\left(-j \pm 1/4 - \frac{1}{2}\frac{\bar\epsilon}{\epsilon_\ell^a}\right). \end{aligned} \tag{B.13}$$

Now, we postulate that the two bifurcation curves $\epsilon_{\ell,m}^a$ and $\epsilon_{\ell,m}^b$ are found when $t_0^2 = t_0^3$ and $t_0^1 = t_0^4$, respectively. From (B.11) and (B.12) we find that these conditions amount to:

$$\theta_\pm^2 - \theta_\pm^3 \approx \frac{1}{\omega}\sqrt{\frac{2\bar\epsilon}{\epsilon_\ell^a}} + \frac{1}{2}\frac{\bar\epsilon}{\epsilon_\ell^a}. \tag{B.14}$$

Substituting (B.13) in (B.14) we obtain:

$$\begin{aligned} \frac{1}{\omega}\bar\epsilon^{3/2}\sqrt{\frac{2}{\epsilon_\ell^a}} + \frac{1}{2}\frac{\bar\epsilon^2}{\epsilon_\ell^a} &\approx \frac{36}{|C(\omega)|\omega^2} \exp\left((-j \pm 1/4)\frac{2\pi}{\omega}\right) \\ &\quad \times \left(\exp\left(-\frac{1}{\omega}\sqrt{\frac{2\bar\epsilon}{\epsilon_\ell^a}}\right) + 2\exp\left(-\frac{1}{2}\frac{\bar\epsilon}{\epsilon_\ell^a}\right)\right) \\ &\approx \frac{108}{|C(\omega)|\omega^2} \exp\left((-j \pm 1/4)\frac{2\pi}{\omega}\right)(1 + O(\sqrt{\bar\epsilon})) \end{aligned}$$

hence

$$\bar\epsilon \approx \left(\sqrt{\frac{\epsilon_\ell^a}{2}}\frac{108}{|C(\omega)|\omega}\right)^{\frac{2}{3}} \exp\left((-j \pm 1/4)\frac{2}{3}\frac{2\pi}{\omega}\right) \tag{B.15}$$

namely,

$$\begin{aligned} \epsilon_{\ell,m}^a - \epsilon_\ell^a &\approx \frac{9^{\frac{1}{3}}36}{|C(\omega)|\omega^{\frac{2}{3}}} \exp\left(-\frac{2}{3}m - \frac{1}{3}l\right)\frac{2\pi}{\omega} \\ \epsilon_{\ell,m}^b - \epsilon_\ell^a &\approx (\epsilon_{\ell,m}^a - \epsilon_\ell^a)\exp\left(-\frac{1}{3}\frac{2\pi}{\omega}\right) \end{aligned} \tag{B.16}$$

or conversely,

$$\begin{aligned} m^a &\approx \left[-\frac{3\omega}{4\pi}\log|C(\omega)|(\epsilon_{\ell,m}^a - \epsilon_\ell^a) - \frac{\omega}{2\pi}\log\frac{\omega}{648} - \frac{1}{2}\ell\right] \\ m^b &\approx \left[-\frac{3\omega}{4\pi}\log|C(\omega)|(\epsilon_{\ell,m}^a - \epsilon_\ell^a) - \frac{\omega}{2\pi}\log\frac{\omega}{648} - \frac{1}{2}\ell - \frac{1}{2}\right] \end{aligned} \tag{B.17}$$

where $[x]$ denotes the integer part of x.

Appendix C. Estimating the escape rates

We derive the 'approximate action formula': let t_i^a, t_i^b, h_i^a, h_i^b denote the crossing times and energies of two homoclinic orbits of order n (so $h_0^{a,b} = h_n^{a,b} = 0, t_0^a < t_0^b$) which are connected to each other by segments of stable and unstable manifolds, enclosing a simply connected domain (i.e. assume there are no additional homoclinic points of order $\leqslant n$ on the connecting segments). The stable (resp. unstable) segment enclosing this domain is given by $(h_0(t_0), t_0)$ values for which $h_n(h_0(t_0), t_0)$ vanishes (resp. $h_0(t_0)$ vanishes). Using the fact that (h_0, t_0) are canonical variables, we conclude that the area enclosed between these segments can be found by integrating $h_0(t_0)\,\mathrm{d}t_0$ for $t_0 \in [t_0^a, t_0^b]$. Approximating the crossing times and energies by the WM, it follows from (4.2) that:

$$h_j(t_0)|_{h_n(t_0)=0} \approx -\epsilon \sum_{i=j}^{n-1} M(t_i) \qquad 0 \leqslant j \leqslant n-1$$

and from (4.2) we find:

$$\frac{\mathrm{d}t_j}{\mathrm{d}t_{j+1}} \approx 1 - P'(h_{j+1})\frac{\mathrm{d}h_{j+1}}{\mathrm{d}t_{j+1}} \qquad 0 \leqslant j \leqslant n-2.$$

Hence,

$$\begin{aligned}
\int_{t_0^a}^{t_0^b} h_0(t_0)\bigg|_{h_n(t_0)=0} \mathrm{d}t_0 &= -\epsilon \int_{t_0^a}^{t_0^b} \sum_{i=0}^{n-1} M(t_i)\,\mathrm{d}t_0 = -\epsilon \int_{t_0^a}^{t_0^b} M(t)\,\mathrm{d}t - \epsilon \int_{t_1^a}^{t_1^b} \sum_{i=1}^{n-1} M(t_i) \frac{\mathrm{d}t_0}{\mathrm{d}t_1}\,\mathrm{d}t_1 \\
&= -\epsilon \sum_{i=0}^{1} \int_{t_i^a}^{t_i^b} M(t)\,\mathrm{d}t - \int_{h_1^a}^{h_1^b} hP'(h)\,\mathrm{d}h - \epsilon \int_{t_2^a}^{t_2^b} \sum_{i=2}^{n-1} M(t_i)\frac{\mathrm{d}t_1}{\mathrm{d}t_2}\,\mathrm{d}t_2 \\
&= \cdots = -\epsilon \sum_{i=0}^{j} \int_{t_i^a}^{t_i^b} M(t)\,\mathrm{d}t - \sum_{i=1}^{j} \int_{h_i^a}^{h_i^b} hP'(h)\,\mathrm{d}h \\
&\quad - \epsilon \int_{t_j^a}^{t_j^b} \sum_{i=j+1}^{n-1} M(t_i)\frac{\mathrm{d}t_j}{\mathrm{d}t_{j+1}}\,\mathrm{d}t_{j+1} \\
&= \cdots = -\epsilon \sum_{i=0}^{n-1} \int_{t_i^a}^{t_i^b} M(t)\,\mathrm{d}t - \sum_{i=1}^{n-1} \int_{h_i^a}^{h_i^b} hP'(h)\,\mathrm{d}h.
\end{aligned}$$

We evaluate $\mu(E_0)$ by using the above formula with $n = 1$, evaluate $e_\ell, e_{\ell+1}$ and $e_\ell + 2$ with $n = 2$ and $e_{2\ell+1}$ with $n = 2$ and $n = 3$. The t_i's and h_i's are found by solving (B.1) and (B.8). The orderings of the integration are determined by the geometry of the manifolds:

$$\mu(E_0) \approx \int_{t_0}^{t_1} h_0(\tau_0)\bigg|_{h_1(\tau_0)=0} d\tau_0 = -\epsilon \int_{t_0}^{t_1} M(t_0)\,\mathrm{d}t_0 = \frac{2\epsilon|C(\omega)|}{\omega} \qquad \text{(C.1)}$$

where $M(t_0) = M(t_1) = 0$ are the two adjacent zeros of the Melnikov function†.

† Equation (C.1) can be derived directly, using the geometrical interpretation of the Melnikov function [6].

Let $\tau_0^i(j), i = 1, \ldots, 4$ be the solutions to (B.1) with index j. Then,

$$e_\ell \approx \int_{\tau_0^3(\ell)}^{\tau_0^1(\ell)} h_0(t_0)\Big|_{h_2(t_0)=0} \mathrm{d}t_0 \qquad .$$

$$e_j \approx \int_{\tau_0^4(j)}^{\tau_0^1(j)} - \int_{\tau_0^3(j)}^{\tau_0^2(j)} h_0(t_0)\Big|_{h_2(t_0)=0} \mathrm{d}t_0 \qquad j = \ell+1, \ell+2. \tag{C.2}$$

The solutions $\tau_0^i(j)$ are found using the Newton method with arc length continuation and bracketing. The initial guess is found using the AWM. The solutions $\tau_0^2(j)$ and $\tau_0^4(j)$ are found first by inverting the monotonic period function P, see (B.2a). Then, we bracket $\tau_0^1(j)$ by $0 < \tau_0^1(j) < \tau_0^2(j)$ (the 0 is replaced by π/ω for $\omega < 1$) and $\tau_0^3(j)$ by $0.5\pi < \tau_0^3(j) < \tau_0^4(j)$ (the 0.5 is replaced by 1.5 for $\omega < 1$).

Finally, we estimate $e_{2\ell+1} = \mu(F^{2\ell+1}(E_0) \cap D_0)$. The set $F^{2\ell+1}(E_0) \cap D_0$ is composed of two arches. One arch is enclosed by segments encircling the origin once. Its area is approximated by (C.2), with $j = 2\ell + 1$. The second (and thicker) arch is enclosed by segments encircling the origin twice before escaping. The end points of these segments are given by t_0^i, the four solutions to (B.8a) with $j = \ell$ and the ℓ in (B.8) replaced by $\ell + 1$. Then, the thicker arch is approximated by

$$\int_{t_0^4}^{t_0^1} - \int_{t_0^3}^{t_0^2} h_0(t_0)\Big|_{h_3(t_0)=0} \mathrm{d}t_0. \tag{C.3}$$

It follows from the geometry of the manifolds that the solutions, t_0^i, obey

$$\tau_0^2(\ell+1) < t_0^1 < t_0^2 < \tau_0^1(\ell) \qquad \text{and} \qquad \tau_0^3(\ell) < t_0^3 < t_0^4 < \tau_0^3(\ell+1) \tag{C.4}$$

and that $t_2^4 < t_2^1 < t_2^2 < t_2^3$. Moreover, by symmetry

$$t_1^2 = t_1^4 = (\ell + 1 + 0.5\delta(\omega))\frac{2\pi}{\omega}. \tag{C.5}$$

Using (C.5), the solutions t_0^2 and t_0^4 of (B.8) are given by the solutions to:

$$t_0 + P(\epsilon C(\omega)\sin(\omega t_0)) = (\ell + 1 + 0.5\delta(\omega))\frac{2\pi}{\omega} \tag{C.6}$$

which are found using the bracketing of (C.4). The solutions t_0^1 and t_0^3 are found by solving (B.8) directly (iterating the WM) and using the accurate bracketing of (C.4) together with the solutions of (C.6).

References

[1] Khakhar D V, Rising H III and Ottino J M 1986 Analysis of chaotic mixing in two model systems *J. Fluid Mech.* **172** 419–51

[2] Davis M J and Skodje R T 1992 Chemical reactions as problems in nonlinear dynamics: a review of statistical and adiabatic approximations from a phase space serspective *Advances in Classical Trajectory Methods* vol 1 (JAI Press) pp 77–164

[3] Escande D F 1988 Hamiltonian chaos and adiabaticity *Plasma Theory and Nonlinear and Turbulent Processes in Physics (Proc. Int. Workshop, Kiev, 1987)* ed V G Bar'yakhtar, V M Chernousenko, N S Erokhin, A G Sitenko and V E Zakharov (Singapore: World Scientific)

[4] Meiss J D, Cary J R, Escande D F, MacKay R S, Percival I C and Tennyson J L 1985 Dynamical theory of anomalous particle transport *Plasma Physics and Controlled Nuclear Fusion Research 1984* vol 3 (Vienna: IAEA) pp 441–8

[5] Davis M J 1985 Bottlenecks to intramolecular energy transfer and the calculation of relaxation rates *J. Chem. Phys.* **83** 1016–31

[6] Rom-Kedar V, Leonard A and Wiggins S 1990 An analytical study of transport, mixing, and chaos in an unsteady vortical flow *J. Fluid. Mech.* **214** 347–94

[7] Troll K 1991 A devil's staircase into chaotic scattering *Physica* **50D** 276–96

[8] Gaspard P and Rice S A 1989 Scattering from a classically chaotic repellor *J. Chem. Phys.* **90**

[9] Lichtenberg A J and Lieberman M A *Regular and Stochastic Motion* (New York: Springer)

[10] MacKay R S, Meiss J D and Percival I C 1984 Transport in Hamiltonian systems *Physica* **13D** 55–81

[11] Knobloch E and Weiss J B 1987 Mass transport and mixing by modulated traveling waves *Phys. Rev.* A **36** 1522

[12] Shlesinger M F, Zaslavsky G M and Klafter J 1993 Strange kinetics *Nature* **363** 31

[13] Meiss J D 1992 Symplectic maps, variational principles, and transport *Rev. Mod. Phys.* **64** 795–848

[14] Meiss J D and Ott E 1986 Markov tree model of transport in area-preserving maps *Physica* **20D** 387–402

[15] Camassa R and Wiggins S 1991 Chaotic advection in Rayleigh Bénard flow *Phys. Rev.* A **43** 774–97

[16] Rom-Kedar V and Wiggins S 1991 Transport in two-dimensional maps: concepts, examples, and a comparison of the theory of Rom-Kedar and Wiggins with the Markov model of MacKay, Meiss, Ott, and Percival *Physica* **51D** 248–66

[17] Rom-Kedar V 1993 The topological approximation method *Transport, Chaos and Plasma Physics (Proc., Marseille)* ed S Benkadda, F Doveil and Y Elskens (Singapore: World Scientific) to be published

[18] Abraham R H and Shaw C D *Dynamics - The Geometry of Behaviour, part 3: Global Behaviour* (Aerial Press)

[19] Birkhoff G D 1950 Nouvelles recherches sur les systemes dynamiques *Collected Works* vol 2

[20] Judd K 1989 The fractal dimension of a homoclinic bifurcation *Preprint;* 1989 The fractal dimension of a homoclinic bifurcation 2: heteroclinic orbits and the duffing system *Preprint*

[21] Ottino J M 1989 *The Kinematics of Mixing: Stretching, Chaos, and Transport* (Cambridge: Cambridge University Press)

[22] Rom-Kedar V 1990 Transport rates of a family of two-dimensional maps and flows *Physica* **43D** 229–68

[23] Wiggins S 1990 *Introduction to Applied Nonlinear Dynamical Systems and Chaos* (Berlin: Springer)

[24] Guckenheimer J and Holmes P *Non-Linear Oscillations, Dynamical Systems and Bifurcations of Vector Fields* (New York: Springer)

[25] Rom-Kedar V 1993 Secondary homoclinic bifurcation theorems *Erg. Theor. Dyn. Syst.* submitted

[26] Elskens Y and Escande D F 1991 Slowly pulsating separatrices sweep homoclinic tangles where islands must be small: an extension of classical adiabatic Theory *Nonlinearity* **4** 615–67

[27] Hillermeier C F, Blümel R and Smilansky U 1992 Ionization of H Rydberg atoms: fractals and powerlaw decay *Phys. Rev.* A **45** 3486–502

[28] Easton R W 1986 Trellises formed by stable and unstable manifolds in the plane *Trans. Am. Math. Soc.* **294** 2

[29] Davis M J, MacKay R S and Sannami A 1991 Markov shifts in the Hénon family *Physica* **52D** 171–8

[30] Chirikov B V 1979 A universal instability of many-dimensional oscillator systems *Phys. Rep.* **52** 263

[31] Zaslavskii G M and Filonenko N N 1968 Stochastic instability of trapped particles and conditions of applicability of the quasi-linear approximation *Sov. Phys.–JETP* **25** 851–7

[32] Rom-Kedar V 1991 Homoclinic structures in open flows *Large Scale Structures in Nonlinear Physics, Proc. Villefranche-sur-mer (Lecture Notes in Physics)* ed J-D Fournier and P-L Sulem (New York: Springer) pp 50–72

[33] Bensimon D and Kadanoff L P 1984 Extended chaos and disappearance of KAM trajectories *Physica* **13D** 82

[34] Kaper T J, Kovacic G and Wiggins S 1990 Melnikov functions, action, and lobe area in Hamiltonian systems *J. Dyn. Diff. Eq.* submitted

[35] Karney C F F 1983 Long time correlations in the stochastic regime *Physica* **8D** 360

[36] Hanson J D, Cary J R and Meiss J D 1985 Algebraic decay in self-similar Markov chains *J. Stat. Phys.* **39** 327–45

[37] Kaper T J and Wiggins 1991 Lobe area in adiabatic systems *Physica* **51D**

[38] Holmes P, Marsden J and Scheurle J 1988 Exponentially small splittings of separatices with applications to KAM theory and degenerate bifurcations *Contemp. Math.* **81** 213–44

[39] Hobson D 1991 An efficient method for computing invariant manifolds of planar maps *J. Comput. Phys.* in press